Article

Borna disease virus docks on neuronal DNA double-strand breaks to replicate and dampens neuronal activity

Cytoplasm

Nucleus

vSPOT

Viral
Proteins

Production
of viral RNAs

Inhibition of
surface
NMDAR

TOP2β

DSB

NMDAR
activation

Epigenetic
remodeling

Reduced neuronal
activity response

BoDV-1

Florent Henri
Marty, Luca
Bettamin, Anne
Thouard, ..., Cécile
Evelyne Malnou,
Daniel Gonzalez-
Dunia, Elsa
Suberbielle

elsa.suberbielle@inserm.fr

Highlights

BoDV-1, its Nucleoprotein
or Phosphoprotein cause
neuronal DNA double-
strand breaks (DSB)

DNA double-strand
breaks co-localize with
BoDV-1 replication
factories

DNA DSB recruits BoDV-1
replication factories and
promotes viral replication

BoDV-1 inhibits neuronal
activity by impeding
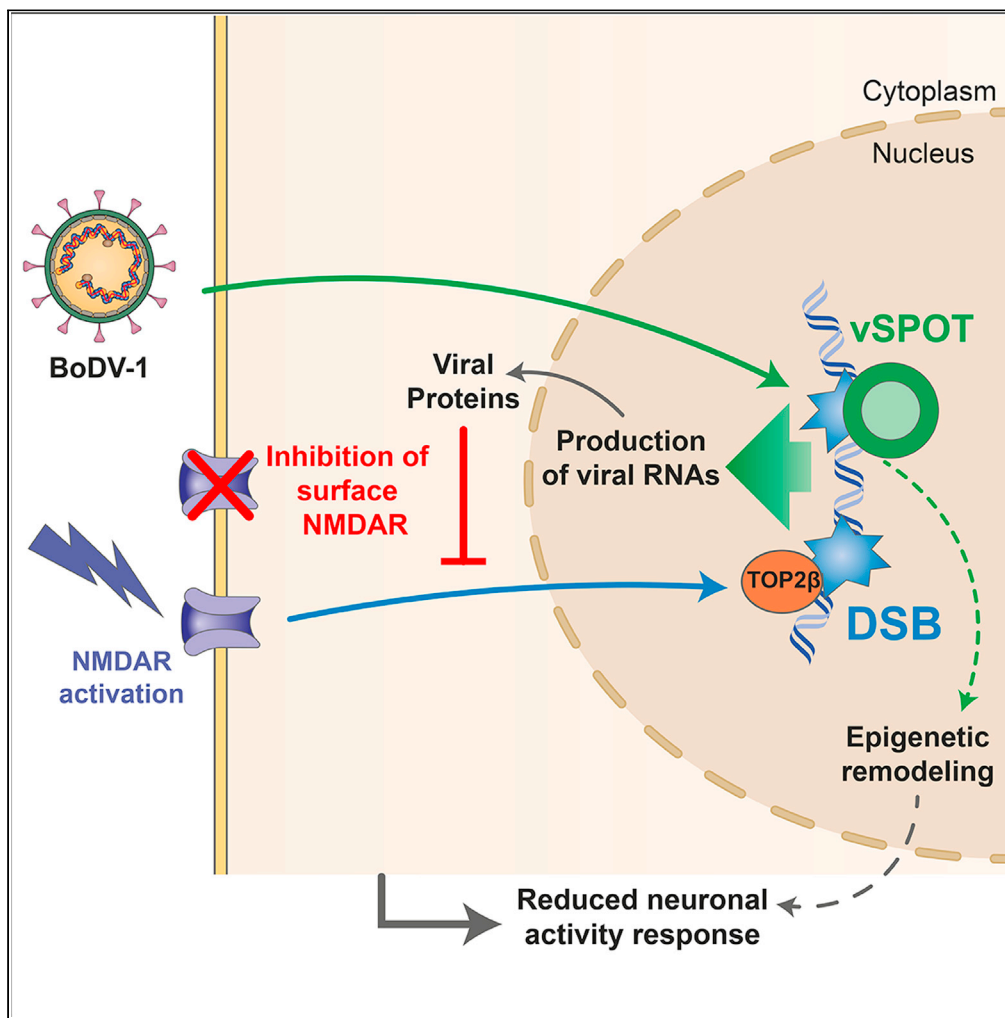surface expression of
GluN2A receptors

iScience

Article

Borna disease virus docks on neuronal DNA double-strand breaks to replicate and dampens neuronal activity

Florent Henri Marty,[1] Luca Bettamin,[1,2] Anne Thouard,[1] Karine Bourgade,[1] Sophie Allart,[1] Guilhem Larrieu,[2] Cécile Evelyne Malnou,[1] Daniel Gonzalez-Dunia,[1] and Elsa Suberbielle[1,3,*]

SUMMARY

Borna disease viruses (BoDV) have recently emerged as zoonotic neurotropic pathogens. These persistent RNA viruses assemble nuclear replication centers (vSPOT) in close interaction with the host chromatin. However, the topology of this interaction and its consequences on neuronal function remain unexplored. In neurons, DNA double-strand breaks (DSB) have been identified as novel epigenetic mechanisms regulating neurotransmission and cognition. Activity-dependent DSB contribute critically to neuronal plasticity processes, which could be impaired upon infection. Here, we show that BoDV-1 infection, or the singled-out expression of viral Nucleoprotein and Phosphoprotein, increases neuronal DSB levels. Of interest, inducing DSB promoted the recruitment anew of vSPOT colocalized with DSB and increased viral RNA replication. BoDV-1 persistence decreased neuronal activity and response to stimulation by dampening the surface expression of glutamate receptors. Taken together, our results propose an original mechanistic cross talk between persistence of an RNA virus and neuronal function, through the control of DSB levels.

INTRODUCTION

The impact of central nervous system (CNS) infections on neuronal physiology represents a fascinating example of host/pathogen interaction (Lathe and St Clair, 2020). In the case of viruses persisting in post-mitotic neurons, neuronal dysfunction upon infection may result from interference with specific cellular pathways. Noteworthy, long-lasting changes in neuronal function caused by neurotropic viruses may result from epigenetic changes triggered in the host cell, even without any associated overt neuronal loss, for which the underlying mechanisms remain largely unknown (Galvan et al., 2015; Tsai and Cullen, 2020). This is indeed particularly relevant when considering that epigenetic marks play a fundamental role in neuronal adaptive responses and cognitive functions (Akbarian et al., 2013; Day and Sweatt, 2011). Among these epigenetic processes, DNA double-strand breaks (DSB) are increasingly recognized as major regulators of neuronal function.

Until recently, DSB were only considered as being deleterious to genome stability and to result in the activation of apoptotic signaling cascades. However, DSB can also occur during physiological conditions, such as meiosis and ontogeny of T and B cells (Alt et al., 2013; Baudat et al., 2013; Bednarski and Sleckman, 2019). Concerning the CNS, notably post-mitotic mature neurons, increasing evidence points to DSB as major regulators of gene expression, by recruiting epigenetic modifiers and by altering the structure of gene promoters. As a matter of fact, the role of neuronal DSB in carving the epigenetic landscape involved in cognition is an emerging area of research. Interestingly, DSB not only accumulate in the brain of mouse models of Alzheimer's disease (Suberbielle et al., 2015) but also occur physiologically in healthy post-mitotic mature neurons upon activation by various sensory or cognitive challenges (Suberbielle et al., 2013). Rapidly and efficiently resolved by the DNA repair machinery, these physiological DSB are not deleterious for neurons and may even contribute to the chromatin remodeling mechanisms that are required for memory acquisition (Madabhushi et al., 2015).

Several viruses can efficiently target factors involved in the production of DSB by endonucleases, their detection, or their repair (Hu et al., 2019; Luftig, 2014; Weitzman and Fradet-Turcotte, 2018). However,

[1]Infinity, Université Toulouse, CNRS, Inserm, UPS, Toulouse, France

[2]LAAS-CNRS, Toulouse, France

[3]Lead contact

*Correspondence: elsa.suberbielle@inserm.fr

https://doi.org/10.1016/j.isci.2021.103621

only a few studies have focused on the impact of RNA viruses on DSB (Chen et al., 2019; Hammack et al., 2019; Hristova et al., 2020; Ledur et al., 2020; Ryan et al., 2016). For *Retroviridae* and *Orthomyxoviridae*, controlling DSB levels is critical to delay the induction of apoptosis (Hristova et al., 2020; Khanna et al., 2010; Koyama et al., 2013; Li et al., 2015; Piekna-Przybylska et al., 2017). Moreover, the role of DSB in the course of these infections has only been studied using mitotic cells. In sharp contrast, studying the responses to DSB in post-mitotic neurons may reveal impaired pathways upon infection, which are key regulators of neuronal function, are not associated to overt neuronal loss, but still induce severe consequences on brain function.

Borna disease virus-1 (BoDV-1) is an ideal model system for this type of investigations. This single-stranded negative persistent RNA virus displays strong neurotropism. BoDV-1 can infect a wide range of vertebrate species, and recent evidence reported the association of BoDV-1 with fatal encephalitis in humans (Finck et al., 2020; Niller et al., 2020; Schlottau et al., 2018). In animal models, BoDV-1 causes behavioral impairment in infected hosts in the absence of overt neuronal loss. Strikingly, it has been shown that BoDV-1 persistence in cell lines results from the interaction of viral ribonucleoparticles (RNPs) with the chromatin (Hirai et al., 2016; Matsumoto et al., 2012). Moreover, both BoDV-1 infection and the viral Phosphoprotein P have been found to contribute to the deleterious impact of this virus on neuronal function (Betourne et al., 2018; Volmer et al., 2006), notably through epigenetic modifications of neuronal chromatin (Bonnaud et al., 2015; Suberbielle et al., 2008). However, the fundamental questions of if and how BoDV-1 may hijack the DNA DSB response in postmitotic neurons have never been addressed.

In this study, we sought to decipher the interplay between BoDV-1 infection of primary cultures of rat neurons and DSB and to unravel its consequences on viral replication and neuronal function. We found that two viral proteins that are part of the RNP are sufficient to elevate DSB levels in neurons and that viral factories benefit from DSB to increase replication. Infected neurons showed impaired electric activity and response to stimulation. Our work provides new clues to understand the unique challenges that a neurotropic RNA virus faces for its persistence in postmitotic cells and illustrates the intricate relationships between neuronal stimulation and replication of an RNA virus.

RESULTS

BoDV-1 infection increases DSB levels in primary neurons

To determine whether BoDV-1 persistence could impact on physiological DSB levels in neurons, we infected primary cultures of hippocampal rat neurons and measured the levels of specific DSB hallmarks in neurons at 13 days post infection (dpi). As previously documented (Hans et al., 2004), neuronal cultures were 100% infected by BoDV-1 at that time point (Figures 1A and S1A). To mark DSB, we first assessed expression of 53BP1, which is recruited specifically to DSB sites, where it forms foci (Anderson et al., 2001; Suberbielle et al., 2013). Because of its critical role in the detection and repair of DSB in post-mitotic cells, 53BP1 displays a neuron-specific characteristic diffuse nuclear staining when assessed by immunofluorescence microscopy, whereas it forms bright fluorescent foci at DSB sites (Suberbielle et al., 2013; Torres et al., 2015) (Figures 1B and S1A). Importantly, this characteristic diffuse nuclear 53BP1 staining is absent in glia, which is useful to discriminate neurons from glia in a culture. We found that BoDV-1 infection increased by 60% the number of neurons displaying 53BP1-positive foci, when compared with mock-infected controls (NI) (Figure 1C). Next, we used Western blot analysis to evaluate phosphorylation levels at serine 139 of Histone 2A variant X (γH2A.X), which is also recruited at DSB sites. Consistent with our analysis of 53BP1, we observed that γH2A.X protein levels were increased in infected neurons compared with mock-infected cultures (Figures 1D and 1E). To confirm that BoDV indeed increased DSB levels and not just 53BP1 foci and γH2A.X levels without a *bona fide* DNA breakage, we assessed the level and severity of DNA fragmentation using single-cell gel electrophoresis, also known as comet assay (Figures 1F–1I). When performed at neutral pH, the comet assay allows measuring DNA DSB (Olive and Banath, 2006; Suberbielle et al., 2013). We found that BoDV-1 infection increased by 46% the percentage of cells with DNA fragmentation (Figures 1F and 1G). As a positive control, we used Etoposide treatment, which increases the endonuclease activity of Topoisomerase 2β, while blocking its ligase function of DNA repair, therefore causing accumulation of DSB (Hu et al., 2019; Madabhushi et al., 2015). Compared with Etoposide, which induced both increased Tail moment and Tail length, BoDV did not alter Tail moment or Tail length, likely reflecting a lower severity of DNA fragmentation (Figures 1H and 1I). We ruled out the hypothesis that the increased DSB levels detected in BoDV-1-infected cultures might result from apoptosis, by performing TUNEL staining analyses, which confirmed that BoDV-1 infection did not lead to neuronal apoptosis (Figure S1B). Next, to test whether increased DSB levels in BoDV-1-infected cultures could be caused by the
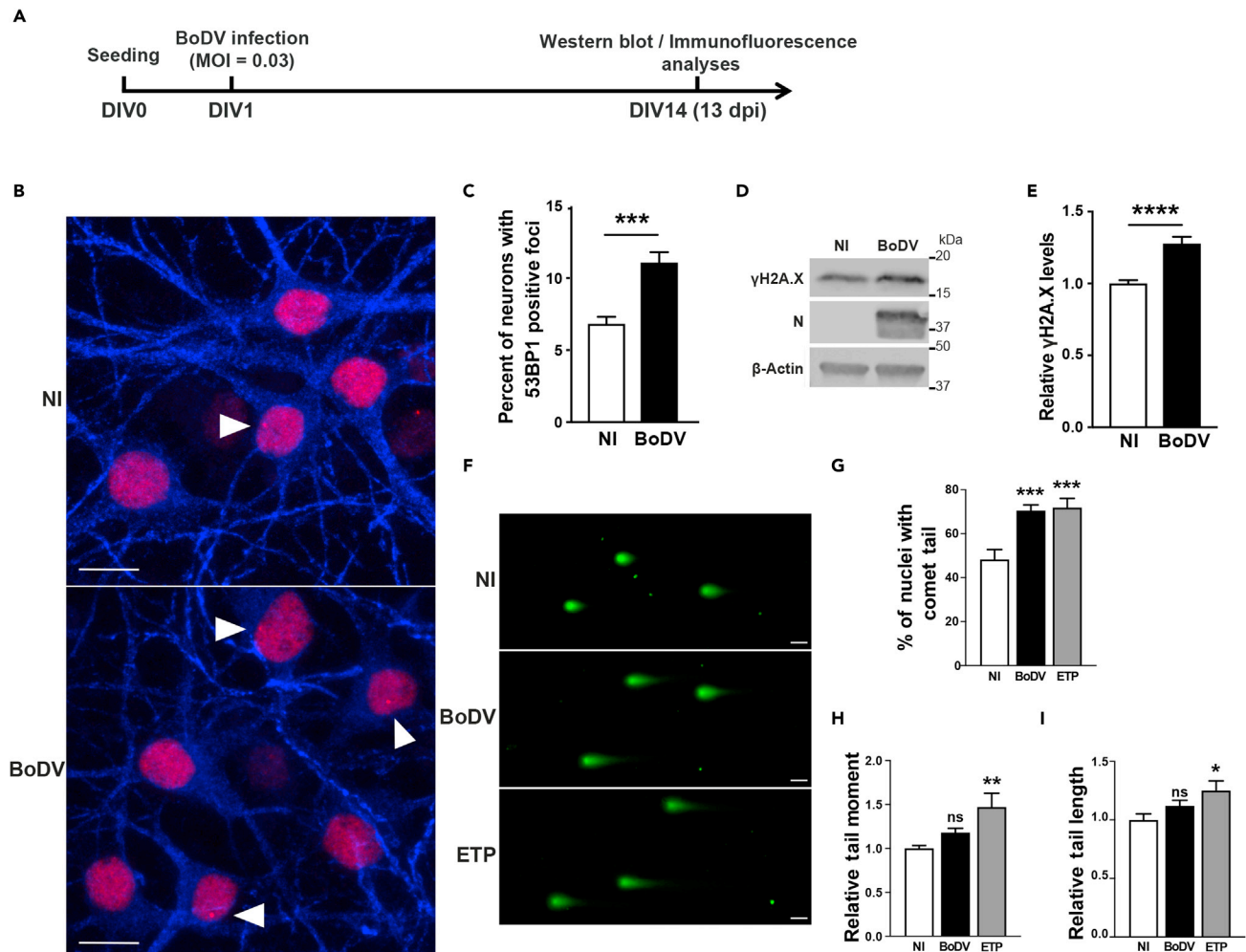
Figure 1. BoDV-1 increases levels of DNA double-strand breaks in primary neurons

(A) Schematic representation of the experimental strategy using primary cultures of rat hippocampal neurons and BoDV-1 infection.

(B) Insets views are displayed from confocal microscopy analysis of 53BP1 staining (red) and MAP2-positive (blue) neurons from BoDV-1 (BoDV) versus non-infected (NI) cultures. Arrows indicate 53BP1-positive foci of DSB. Scale bar: 10 μm.

(C) Numbers of neurons with 53BP1-positive foci were counted and are expressed as average percentages of foci-positive neurons. A total of 2,358 NI- and 2,697 BoDV-1 infected neurons were observed in n = 2–3 fields on 4–6 coverslips per condition from 3 independent experiments. ***p = 0.001 versus NI by unpaired t test.

(D-E) Levels of the DSB marker γH2A.X were determined by Western blotting.

(D) A Western blot illustrating particularly strong increase in γH2A.X signals upon infection. Nucleoprotein (N) and β-actin levels were also detected.

(E) Quantitation of Western blot signals. The average γH2A.X to β-actin ratio in non-infected cultures was defined as 1.0. n = 2–6 wells per condition from 7 independent experiments. ****p < 0.0001 versus NI by unpaired t test with Welch correction.

(F-I) Cell nuclei isolated from 14-DIV primary mixed cultures of hippocampal neuron homogenates were assessed for DNA fragmentation levels by the comet assay at neutral pH.

(F) Representative images of cell nuclei from non-infected (NI), BoDV-infected (BoDV) cultures or as a positive control, after 5 h incubation with 0.5 μM Etoposide (ETP). Images were captured by fluorescence microscopy. Scale bar: 10 μm.

(G) Quantification of the percentage of nuclei with comet tails, which are indicative of DSB. For each condition, a total of 1,325–2,190 nuclei were inspected and scored.

(H) Tail moment, indicating the severity of DNA fragmentation as a function of the number of fragments produced and the lengths of the fragments, was measured for each cell showing a comet.

(I) Tail length, indicating the extent of DNA fragmentation, was measured for each cell showing a comet. Tail moment and length are expressed as normalized on the average tail moment/length for the NI measured for each experiment. n = 6–8 wells per condition from 4 independent experiments. *p < 0.05, **p < 0.01, ***p < 0.001 versus leftmost bar (Dunnett post hoc test). Bars represent means ± SEM.
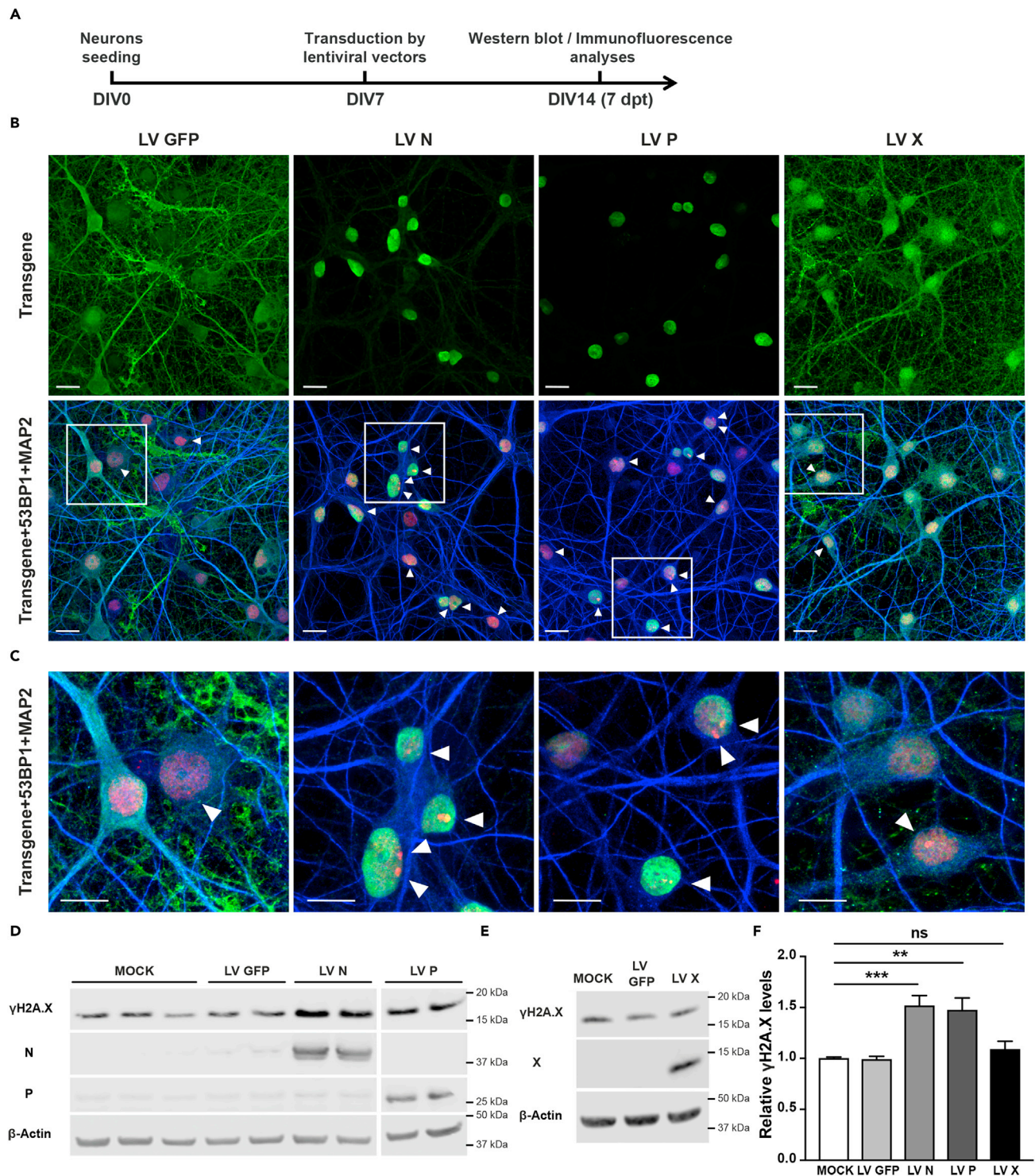
Figure 2. BoDV-1 Nucleoprotein N and Phosphoprotein P increase DSB levels in neurons

Primary cultures of rat neurons were transduced 7 days after seeding (DIV) by lentiviral vectors (LVs) to express BoDV-1 Nucleoprotein (N), Phosphoprotein (P), X protein (X), or green fluorescent protein (GFP) as a control. Wells that were not transduced are shown as mock. Seven days post transduction (dpt), expression of these proteins and DSB markers was assessed by confocal microscopy (B, C), and their levels were assessed by Western blot analysis (D-F). (A) Schematic representation of the experimental strategy.

Figure 2. *Continued*

(B) 53BP1 staining (red) in N- versus P- versus X- versus GFP-expressing (green) and MAP2-positive (blue) neurons was visualized by confocal microscopy. Scale bar: 20 μm.

(C) Inset views from (B) of the triple staining are shown at higher magnification. Arrows indicate DSB foci. Scale bar: 10 μm.

(D-F) Levels of the DSB marker γH2A.X were determined by Western blotting. (D-E) Representative Western blots are shown. (F) Quantitative analysis of the Western blot signals. The average γH2A.X to β-actin ratio in mock-transduced cultures was defined as 1.0. n = 2–4 wells per condition from 5–16 independent experiments. ns, non-significant ***p < 0.001, **p < 0.01 versus mock by Dunnett post hoc test with Welch correction. Bars represent means ± SEM.

release of soluble factors in the culture medium upon infection, we swapped medium between BoDV-1- and mock-infected cultures (Figure S2). We observed that incubating non-infected neurons for 5 h with the medium of BoDV-1-infected neurons did not increase γH2A.X levels, whereas at that time, the incubation of neurons with either amyloid-β oligomers or pro-inflammatory cytokines was sufficient to induce DSB (Suberbielle et al., 2013 and data not shown). Hence, the increased DSB levels likely directly result from the presence of BoDV-1 in neurons.

BoDV-1 Nucleoprotein and Phosphoprotein induce DSB in neurons

To assess whether the singled-out expression of any viral protein could similarly increase DSB levels in neurons, we transduced primary neurons with lentiviral vectors (LVs) expressing two main components of the BoDV-1 ribonucleoparticle, the Nucleoprotein (N) and Phosphoprotein (P), as well as the non-structural X protein. We explored DSB levels 7 days post transduction, at 14 days *in vitro* (DIV), to allow both completion of post-integration DNA repair of the lentiviral vectors (Skalka and Katz, 2005) and good expression of the transgene proteins (Figure 2). After confirming the expected partly nuclear pattern of expression of the green fluorescent protein (GFP), N, P, and X in neurons by immunofluorescence confocal microscopy, we could already detect increased levels of 53BP1 foci in neurons transduced with LV N or LV P, but not with LV GFP or LV X, with a trend to display more than one focus per cell (Figures 2B and 2C). Likewise, Western blot analyses showed that expression of either N or P increased γH2A.X levels in neurons by 50%, whereas X or GFP did not lead to any change in DSB levels (Figures 2D–2F). By comet assay, compared with LV GFP, the singled-out expression of N or P proteins increased DNA fragmentation by, respectively, 68% and 33% (Figures S3A and S3B). Noteworthy, LV N caused higher severity of DNA fragmentation, as shown by significantly increased Tail moment and Tail length of the comets when compared with LV GFP (Figures S3A, S3C, and D).

BoDV-1 nuclear viral factories are located in the direct vicinity of neuronal DSB

Having shown that N and P, which are two main components of BoDV-1 viral factories, called vSPOT (for viral SPeckles Of Transcripts) induce DSB in neurons, we decided to explore the spatial relationship between DSB and vSPOT in the nuclei of neurons. To this aim, we analyzed neuronal staining by super-resolution confocal microscopy using STED technique (Figure 3). This technique allows one to reach a resolution of 40 nm. We found that vSPOT events were colocalized at 63.8% ± 21.4 SD with a 53BP1-positive focus when both events could be visualized in the same neuron (Figures 3B–3D), and as illustrated in the 3D reconstruction of a nucleus structure and animated view (Figure 3C and Video S1). When they were not co-localized, there was no specific pattern in the distance between vSPOT and 53BP1-positive foci (Figures 3A and 3D). To further confirm that vSPOT co-localized at DSB sites, we also performed 3D-STED analyses of BoDV N and γH2A.X. Being a core histone variant, γH2A.X is directly bound to DNA at DSB sites and is considered as the earliest marker of a DSB (Baldock et al., 2015). Using these co-stainings, we observed that all vSPOT co-localized with a γH2A.X-positive focus (Figures 3E, 3F, and S4 and Video S2). We also confirmed that 85% of γH2A.X-positive foci were also co-stained with 53BP1, both in BoDV-infected neurons and in non-infected controls (Figure S4C), as previously already demonstrated *in vivo* (Suberbielle et al., 2013). Altogether, our results indicate that vSPOT preferentially locate at the level of DSB in the chromatin of neurons.

Etoposide-induced DSB activate BoDV-1 replication

The close spatial relationship between vSPOT and DSB foci led us to hypothesize that DSB may be used as hubs for the virus to replicate and may thereby modulate viral replication. Therefore, to test if DSB may promote or impede viral replication upon BoDV-1 persistent infection, we increased steady-state DSB levels in neurons using Etoposide (Figure 4). First, we infected primary cultures of neurons with BoDV-1 at 7 DIV, to allow viral spread in already mature neuronal networks able of spontaneous activity. Neurons were treated with varying concentrations of Etoposide 2 days later, to analyze a potential recruitment of BoDV-1 viral
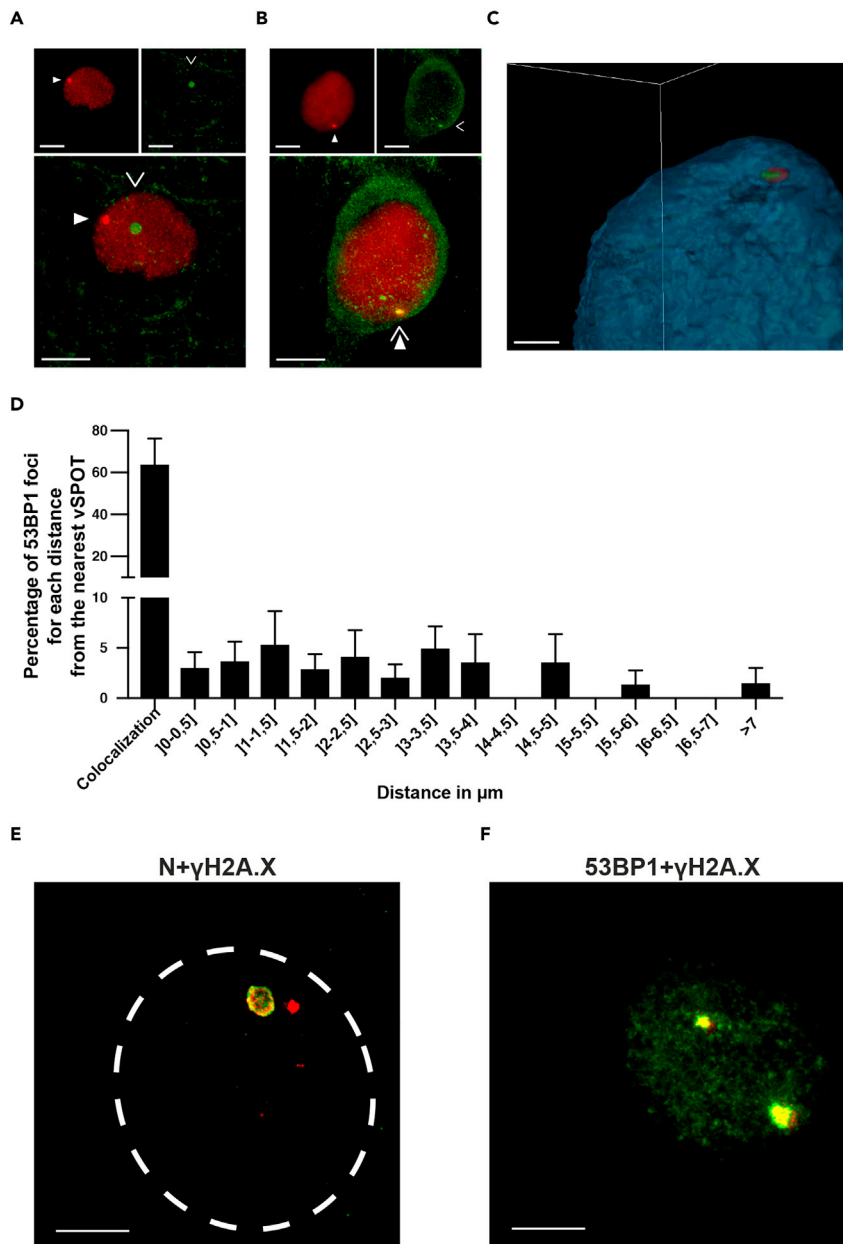
Figure 3. BoDV-1 vSPOT and DSB are strongly colocalized in infected neuronal nuclei

Super-resolution confocal microscopy analysis was performed by STED technology on BoDV-1-infected rat neurons at 13 dpi.

(A and B) Representative 2D-STED images of 53BP1-positive (in red) DSB foci (plain arrow), and Nucleoprotein-positive (in green) vSPOT (empty arrow) staining and merged images of the same confocal planes. (A) Representative example of a neuronal nucleus with no colocalization between DSB and vSPOT. (B) Representative example of a neuronal nucleus with fully colocalized DSB and vSPOT. Scale bar: 5 μm.

(C) Representative 3D-STED 3D reconstruction view of a nucleus (in blue) with colocalized 53BP1-positive DSB foci (in red) with Nucleoprotein-positive vSPOT (in green). The full 3D reconstruction can be observed as a 3D animation in Video S1. Scale bar: 2 μm.

(D) Quantitative analysis of the distribution of neuronal nuclei with 53BP1-positive foci and their nearest vSPOT in function of the distance between these two events, expressed as the average percentage for each distance interval measured. n = 22–61 nuclei analyzed per experiment from 3 independent experiments.

(E and F) Representative 2D-STED images are displayed in (E) γH2A.X-positive DSB foci (red) colocalized with Nucleoprotein-positive (green) vSPOT in the nucleus (dashed circle) of a neuron from a BoDV-1-infected culture. A full 3D reconstruction can be observed as a 3D animation in Video S2; in (F) γH2A.X-positive foci of DSB (red) colocalized with 53BP1-positive foci of DSB (green) in the nucleus of a BoDV-infected neuron. General corresponding confocal views are displayed in Figure S4. Scale bar: 5 μm. Bars represent means ± SEM.
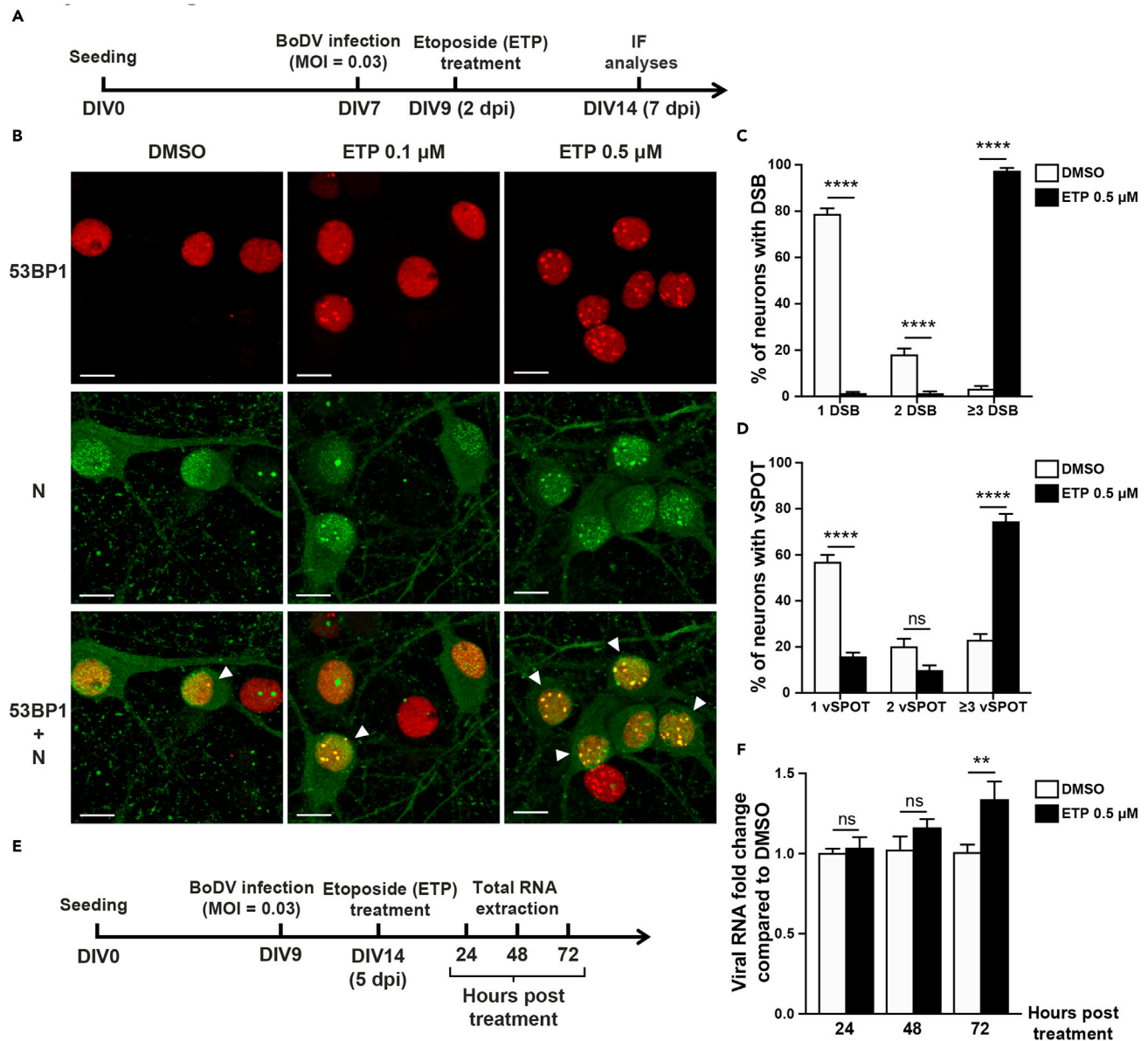
Figure 4. Induction of DSB in neurons by Etoposide increases numbers of colocalized DSB/vSPOT per neuron and viral RNA replication

(A) Schematic representation of the experimental strategy. Primary cultures of rat hippocampal neurons were infected by BoDV-1 and treated with the DSB-inducing agent Etoposide (ETP) or its vehicle DMSO, followed by immunofluorescence analysis.

(B–D) The numbers of DSB and vSPOT and the levels of colocalization of these two nuclear events were assessed by manual counting following immunofluorescence staining of 53BP1-positive foci of DSB (in red), and Nucleoprotein-positive (N) vSPOT (in green) analyzed by confocal microscopy. (B) Representative confocal images of DSB foci, vSPOT, and their colocalization (arrow), for experiments using 0.1 or 0.5 μM Etoposide, or vehicle-treated (DMSO) cultures. Scale bar: 10 μm. (C) Distribution as percentage of the counts of infected neurons displaying DSB foci in three categories (1, 2, or ≥3 DSB/cell) depending on the numbers of foci per nucleus observed. (D) Distribution of the counts of the same neurons displaying vSPOT in three categories (1, 2, or ≥3 vSPOT/cell) depending on the numbers of events per nucleus observed. n = 22–44 neurons analyzed from 2 coverslips per condition, from 3 independent experiments. ns, non-significant, ****$p < 0.0001$ by multiple t test.

(E and F) Quantitative analysis by RT-qPCR of BoDV-1 viral RNA levels in rat hippocampal neurons, after infection by BoDV-1 and at 3 different times post treatment with Etoposide (ETP) or vehicle (DMSO). (E) Schematic representation of the experimental strategy. (F) Changes in RNA levels are expressed as compared with the DMSO condition, for which the average ΔΔCt (normalized on GAPDH) was set to 1. n = 2 wells analyzed each in duplicates, per condition from 4 independent experiments. ns, non-significant, **$p < 0.01$ by Bonferroni post hoc t test. Bars represent means ± SEM.
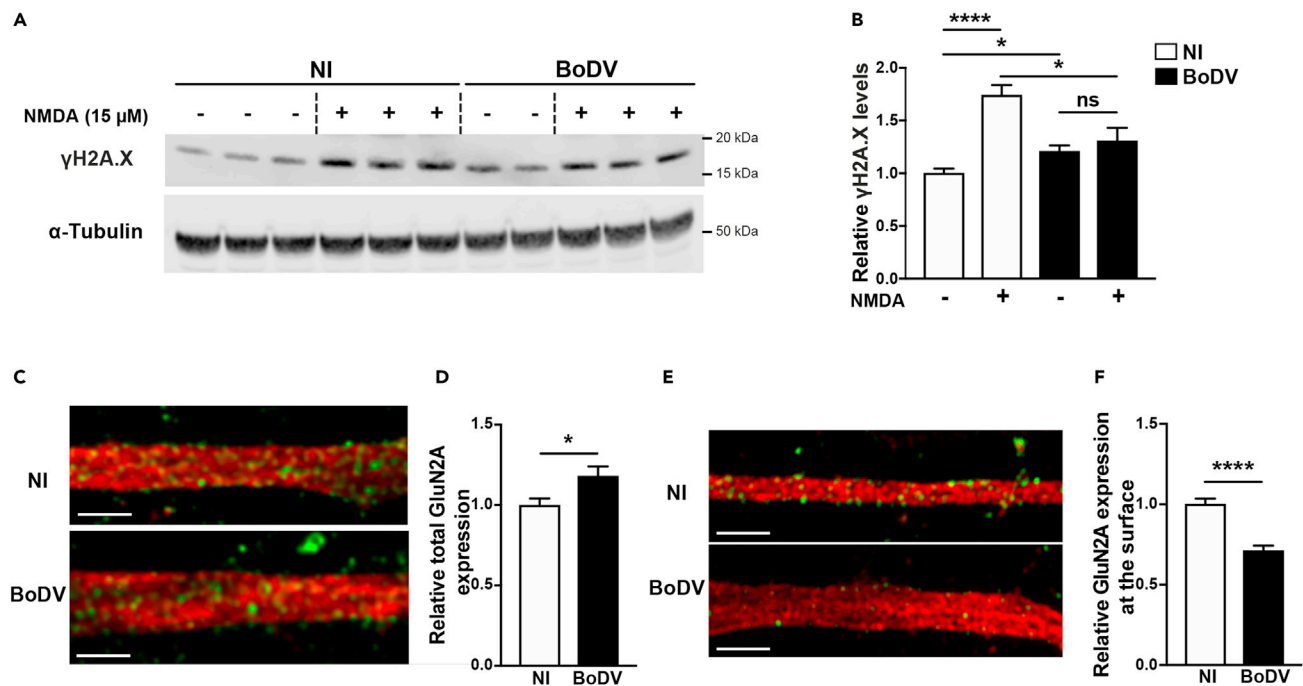
Figure 5. Persistent BoDV-1 infection prevents activity-induced DSB in neurons by decreasing surface expression of NMDA receptors (NMDARs)

(A and B) When primary neuronal cultures were fully and steadily infected (BoDV), neurons were incubated with the NMDARs selective agonist NMDA (+) or vehicle (−) for 30 min. DSB levels were assessed by Western blot analysis. (A) A representative Western blot is shown. (B) Quantitation of Western blot signals. The average γH2A.X to α-Tubulin ratio in non-infected (NI) cultures was defined as 1.0. n = 2–3 wells per condition from 8 independent experiments. (C–F) Total (C–D) and surface (E-F) expressions of the GluN2A subunit of NMDARs were quantified by immunofluorescence staining followed by confocal microscopy analysis. (C, E) Representative high-resolution images obtained using Airyscan 2 technology are shown of total (C) and surface (E) GluN2A signals (in green) in dendrites (MAP2, red) from BoDV-1 versus non-infected (NI) neurons at 16 DIV. Scale bar: 2 μm (D, E) Quantitative analyses of total (D) and surface (F) GluN2A clusters of signals are shown. The average GluN2A signal measured in each experiment in NI cultures was defined as 1.0. In average, 74 versus 84 (NI versus BoDV) dendrites were assessed for surface expression of GluN2A and 102 versus 94 (NI versus BoDV) dendrites for total expression of GluN2A. n = 3 independent experiments. ns, non-significant, *$p < 0.05$, ****$p < 0.0001$ by Tamhane T2 post hoc t test with Welch correction (B), or by unpaired t test (F). Bars represent means ± SEM.

factories to newly induced DSB (Figure 4A). With this experimental setup, we first evidenced a dose-dependent increase in the number of neurons with 53BP1-positive foci and an increase in the number of foci per nucleus (Figures 4B, 4C, and S5). Strikingly, this increase in DSB was associated with increased numbers of vSPOT per cell (Figure 4B). For instance, infected neurons exposed to 0.5μM Etoposide displayed increased numbers of DSB foci (Figures 4B and 4C) and of vSPOT (Figures 4B and 4D) per cell compared with vehicle-treated controls, together with a 1.8-fold increase in the number of neurons with a vSPOT colocalized with a DSB. vSPOT were mostly co-localized with 53BP1-positive foci and the percentage of colocalization events increased by 66.4%. Hence, induction of multiple DSB in neurons promotes the assembly of viral factories. Next, to determine whether these increased numbers of vSPOT also resulted in accrued replication of the viral RNA, we performed RT-qPCR. Incubating neurons with 0.5 μM Etoposide starting 5 days post infection for various periods of time (Figure 4E) allowed us to determine that increasing the number of DSB and viral factories in neurons accrued the replication of the viral RNA by 33%, most significantly after 72 h of incubation with Etoposide (Figure 4F). Together, these results show that increasing DSB in neurons by Etoposide treatment promotes assembly of viral factories in contact to these newly formed DSB and stimulates viral replication.

BoDV-1-infected neurons do not respond to NMDA stimulation of activity

It has been shown that stimulation of glutamatergic N-methyl D aspartate receptors (NMDARs) at the surface of neurons with their agonist (NMDA) causes transient increases in DSB levels in neurons (Crowe et al., 2006; Madabhushi et al., 2015; Suberbielle et al., 2013). This led us to explore the impact of BoDV-1 neuronal infection on the DSB response after mild stimulation with NMDA. Consistent with previous reports (Crowe et al., 2006; Madabhushi et al., 2015; Suberbielle et al., 2013), exposure of uninfected neurons
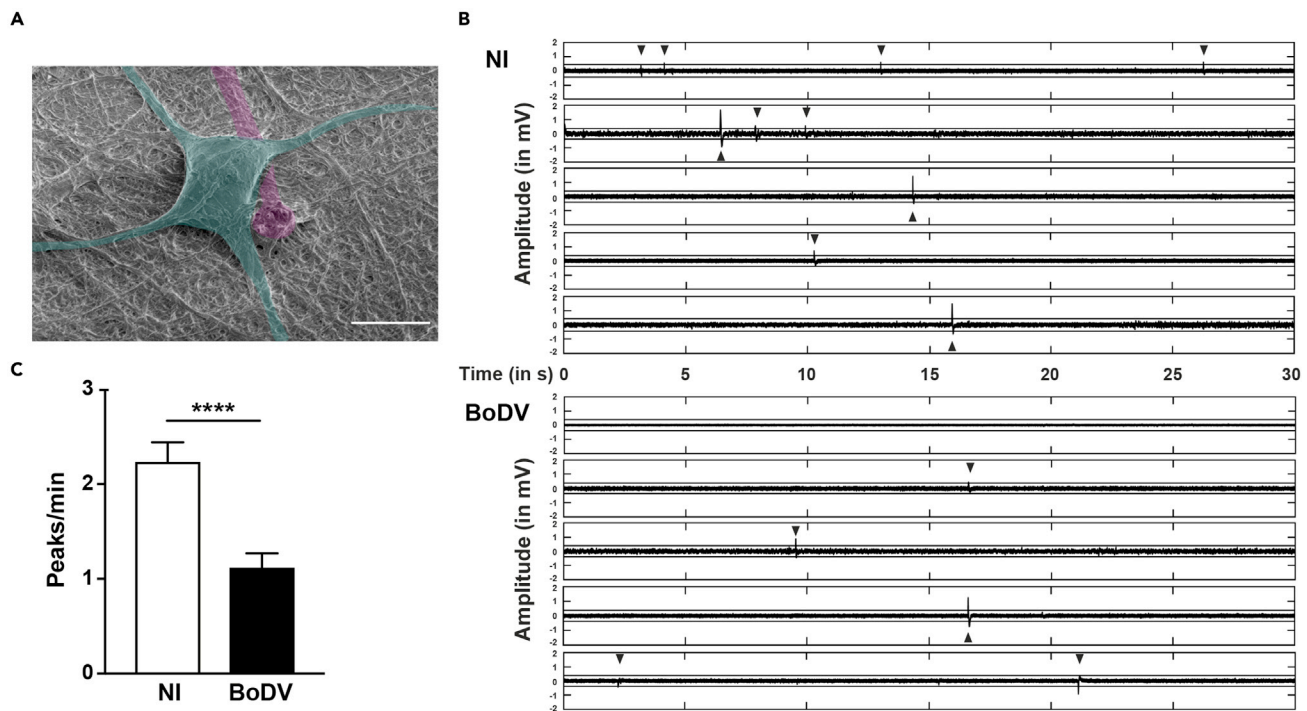
Figure 6. Intrinsic spontaneous neuronal activity is lowered by BoDV-1 infection

Primary cultures of rat neurons were grown on nanoelectrode arrays allowing single-cell recordings from 60 nano-electrodes at 16 dpi.

(A) A neuron cell body and its neurites (green) contacting a nano-electrode (magenta) is shown as observed at high magnification by electron microscopy. Scale bar: 10 μm.

(B) Spontaneous neuronal activity was recorded for 3 min every 15 min, 5–6 times for each electrode. Representative traces for NI and BoDV-1-infected neurons are shown. Each arrow shows a peak above the amplitude threshold of intrinsic electric activity recorded by the electrode.

(C) The average number of peaks of spontaneous intrinsic activity was automatically counted by a home-made algorithm and represented per minute of recording for BoDV-1-infected versus non-infected neurons (NI). n = 1 well per condition from 3 independent experiments. ****p < 0.0001 vs. NI by unpaired t test. Bars represent means ± SEM.

to NMDA caused a 75% increase in DSB levels 30 min post treatment (Figures 5A and 5B). In absence of NMDA treatment, BoDV-infected neurons displayed a significant 20.7% increase in γH2A.X levels, similarly to Figure 1. In contrast, NMDA treatment of BoDV-1-infected neurons failed to further increase DSB levels (Figures 5A and 5B). This result suggests that BoDV-1 infection may interfere with signaling pathways that convey the signal of glutamatergic stimulation from the neuronal cell surface to the nucleus.

To explore the underlying mechanisms of this interference, we first asked whether BoDV-1 infection of neurons may alter the cell surface distribution of NMDAR. We performed immunocytochemistry staining followed by confocal analyses of the surface expression of GluN2A, the most commonly expressed NMDAR subunit in mature excitatory neurons (Wyllie et al., 2013) (Figures 5E, 5F, and S6). We detected a 30% decrease in surface expression of GluN2A on BoDV-1-infected neuronal dendrites compared with non-infected neurons, whereas total levels of GluN2A were slightly increased by BoDV-1 infection (Figures 5C and 5D). Hence, these findings show that once neurons are steadily infected by BoDV-1, surface expression of NMDAR is inhibited, suggesting that the virus may dampen neuronal activity.

BoDV-1-infected neuronal networks display altered spontaneous electric activity

The accumulation of DSB in neurons has been previously shown to cause neuronal dysfunction, notably by interfering with the expression of activity-related genes. Thus, accumulation of DSB due to BoDV-1 infection may durably alter neuronal function and impact on electric activity. To test this hypothesis, we used a novel device, which has been recently implemented in our laboratory, to measure the spontaneous electric activity of neuronal network at the single neuron level, using nanoelectrode arrays (Figures 6A and S7). Using this setup, we first observed that fully BoDV-1 infected cultures displayed on average a 25% decrease in the number of active electrodes compared with non-infected controls (Figures 6A and Table 1). There were

Table 1. Active electrode in infected or non-infected neurons

	NI (%)	BODV (%)	Ratio BODV/NI
EXPERIMENT 1	50.0 (n = 58)	39.7 (n = 58)	0.794
EXPERIMENT 2	90.7 (n = 54)	63.8 (n = 58)	0.703
EXPERIMENT 3	88.9 (n = 54)	68.4 (n = 57)	0.769
MEAN ± SD	77.1 ± 23.6	57.3 ± 15.4	**0.755 ± 0.047***

For each experiment, active electrodes are expressed as percentage of total electrode included (n). The mean (in bold) of the ratios is compared with theoretical value of 1 (no difference) by one sample t test, *p < 0.05.

no noticeable differences between the two conditions in terms of the morphology of neuronal networks, as observed by scanning electron microscopy (Figure S7). Finally, we designed a tool to count the numbers of peaks of voltage potentials above the baseline threshold of each electrode (Figure 6B). Using this tool, we found that BoDV-1 infection decreased the number of peaks/min by 50% compared with non-infected cultures (Figures 6B and 6C). Thus, BoDV-1 infection of neurons impairs spontaneous electric firing within neuronal networks, which likely results from the decreased surface expression of GluN2A.

DISCUSSION

Our study shows that BoDV-1 infection elevates steady-state DSB levels in primary neurons. This is directly due to the presence of the virus in the neurons and could also be reproduced by the singled-out expression of N and P proteins, two main components of the nuclear viral factories. We also demonstrate the close topological association between viral factories attached to the chromatin and DSB and provide evidence suggesting that BoDV-1 may use proteins critically involved in the DSB-damage response as "docking platforms" to facilitate its replication. On the neuronal side, we show that BoDV-1 impairs neuronal firing and decreases surface localization of glutamatergic NMDAR.

We only observed a mild increase in DSB marker levels, revealed by a limited number of 53BP1-positive or γH2A.X-positive foci per neuron, and no significant trends in increase in comet tail moments or lengths in BoDV-infected cultures compared with controls. Because DNA DSB response triggers apoptosis when the severity of the damage is too important to be repaired, our data are consistent with our TUNEL assay results, as well as with our previous demonstrations that BoDV-1 is indeed non-cytolytic in neurons (Hans et al., 2004).

Our study therefore uncovers the first example of an actively replicating RNA virus able to manipulate the DSB neuronal responses to favor the assembly of viral replication complexes and viral persistence, without causing any overt neuronal death. This is in sharp contrast with the situation observed with *Orthomyxoviridae*, the other family of negative-sense RNA genomes replicating in the nucleus, which induces DNA damage related to cellular death (Khanna et al., 2010; Li et al., 2015). Likewise, dysregulated DNA DSB responses for viruses generally lead to either apoptosis or oncogenesis (Chen et al., 2019; Hristova et al., 2020; Ledur et al., 2020; Luftig, 2014; Patra et al., 2020; Ryan et al., 2016; Weitzman and Fradet-Turcotte, 2018). The only viral example comparable with our findings can be found for the control of latency, *e.g.*, with no viral production, of Herpes simplex viruses, which modulate Topoisomerase 2beta activity to maintain latency (Hu et al., 2019).

Our data reveal a tight relationship between viral replication and DSB production. In particular, the topological relationship between vSPOT and DSB foci is striking: to our knowledge, such a tight contact between host DNA DSB and viral RNA genome has never been described to date. Noteworthy, by super resolution confocal STED microscopy, which allows one to reach a resolution as low as 40 nm, colocalized DSB foci and vSPOT were interwoven. Thus, DSB and associated DSB response molecules may form a docking site for vSPOT. This hypothesis is further supported by our results on Etoposide-treated neurons: inducing new DSB rapidly recruits foci-colocalized vSPOT. This raises the question of how BoDV RNP may bind to DSB sites. One possible explanation is that it may result from the direct interactions between BoDV-1 P and N with chromatin-binding proteins, which, to date, have only been identified in replicating cell lines but not in neurons. Of note, High-mobility group binding protein 1 (HMGB1), Poly-ADP-ribose polymerase 1 (PARP-1), and core histones H3, H2A, and H2B interact with P and N, respectively (Matsumoto et al., 2012). Interesting, HMGB1, a minor groove binder, and PARP-1, a chromatin-decompaction enzyme, play roles in DNA repair and their

levels and activities are altered with age in neurons and inversely correlate with DSB accumulation (Enokido et al., 2008; Mandke and Vasquez, 2019; Mao and Zhang, 2021).

Another interesting finding is that the colocalization between DSB markers and vSPOT is total when assessed with γH2A.X, whereas it seems to obey an "all or nothing" rule when detected with 53BP1. Indeed, if most DSB foci co-localize with at least one vSPOT, when no colocalization is evidenced, the distance between the two becomes variable. These observations may result from differences between the kinetics of DSB generation and resolution and kinetics of viral replication. Indeed, γH2A.X is the earliest protein to detect and signal DSB to the repair machinery. The histone variant H2A.X is regularly distributed in the chromatin and becomes phosphorylated (to become γH2A.X) within minutes upon the induction of DSB. In contrast, 53BP1 is specifically recruited to γH2A.X-positive DSB and remains on the chromatin until complete repair of the break. Together with results obtained with Etoposide-induced DSB, our data suggest that recently formed vSPOT are rapidly and preferentially recruited to newly formed and pre-existing DSB, which may, in turn, be stabilized by the vSPOT. This hypothesis would partly explain why at any moment only a mild increase in DSB levels is observed, even if the culture is fully infected. The apparent steady replication of BoDV-1 in neurons, with continuous expression of viral proteins and assembly of viral replication complexes (Cubitt and de la Torre, 1994; Gonzalez-Dunia et al., 1996), may seem contradictory with the non-cytolytic nature of this infection, suggesting unknown mechanisms of control between the host cell and the pathogen. Here, our findings suggest a new mechanism involving a feedback loop between viral replication and excitatory glutamate signaling pathways: the direct trigger of Topoisomerase 2β-dependent DSB, which would increase BoDV-1 replication. Indeed, Etoposide does not directly generate DSB. Rather, it prevents their repair through the inhibition of the ligase activity of Topoisomerase 2β (Hu et al., 2019; Madabhushi et al., 2015). On the other hand, at steady state, infected neurons would display lower current frequencies and be less electrically active. Consistent with this hypothesis, we observed that incubating infected neurons with NMDA to stimulate NMDA receptors, receptors that induce DSB by stimulating Topoisomerase 2β endonuclease activity (Madabhushi et al., 2015), did not result in further increase in DSB, indicating that BoDV-1 likely uncouples NMDARs from their signaling to the generation of new physiological DSB. At the molecular level, this uncoupling may result from the decreased cell surface expression of NMDAR, as evidenced in our study with their core subunit GluN2A. This finding is in line with our previous description that BoDV-1 P protein inhibits protein kinase C (PKC) activity and the subsequent phosphorylation of its target SNAP-25 (Betourne et al., 2018). Indeed, considering that PKC activity and SNAP-25 play critical roles in the maintenance of NMDAR at the neuronal cell surface (Lau et al., 2010; Vieira et al., 2020), our results suggest that BoDV-1 P protein may shut off pathways that cause activity-dependent DSB, while increasing DSB levels in the context of BoDV-1 infection. Thus, the P protein may play a pivotal role not only in the regulation of viral replication but also in neuronal activity. The dual role of the P protein in causing limited DSB damage by controlling neuronal activity is indeed supported in our study by comet assays results. Contrary to N protein, which alone drives both increases in proportions of cells with DNA fragmentation and aggravation of the severity of the fragmentation, the P protein, however, impacts on the proportion of DSB-bearing cells without affecting their severity. This suggests that P stands on the way of the resolution of an otherwise naturally DSB-inducing pathway spontaneously ongoing in neuronal cultures. Therefore, we could envision that neuronal activity and associated DSB may promote docking of vSPOT and favor the early stages of neuronal infection. Next, this would lead to the production of viral factors, including P, which would shut off activation of the neurons, thereby putting a brake on DSB production and limiting overloading the neuron with viral materials, which could trigger apoptosis.

Finally, even limited numbers of DSB have been shown to critically impact on cell function (Madabhushi et al., 2015; Suberbielle et al., 2013; van den Berg et al., 2018). For instance, activity-induced, Topoisomerase 2β-dependent neuronal DSB are sparse, but they target genomic regions that mainly code for survival signals and activity-related proteins (Madabhushi et al., 2015). Likewise, only few 53BP1-positive foci are observed in neuronal nuclei of a mouse model of Alzheimer's disease; yet, they seem sufficient to cause cognitive decline (Suberbielle et al., 2013, 2015). In the recent years, the idea has emerged to consider neuronal DSB as key epigenetic processes regulating gene expression in neurons. In these non-dividing cells that establish lifelong specialized networks, while remaining able of a high degree of adaptability called plasticity, epigenetic mechanisms are critical regulators. As a result, epigenetic processes of the host cell are also often hijacked by persistent viruses (Bonnaud et al., 2016; Lange et al., 2020; Tarakhovsky and Prinjha, 2018) and BoDV-1 is no exception: our group and others identified BoDV-1 P-mediated

interference with acetylation of Histone H2B and H3 (Bonnaud et al., 2015; Jie et al., 2018). Because DSB can be induced by both P and N proteins, and early DSB accumulation in neurons increases Histone H3 lysine 9 dimethylation (Suberbielle et al., 2015), which corresponds to inhibitory signals of gene expression, it is tempting to speculate that DSB and their signaling may play an upstream role in the further deacetylation of histones.

Because increasing evidence has documented human cases of BoDV-1 infection and encephalitis following immunosuppressive treatment, notably in solid-organ transplant recipients (Finck et al., 2020; Korn et al., 2018; Niller et al., 2020; Schlottau et al., 2018), this indicates that BoDV-1 may persist almost silently in the human immunocompetent brain. Thereof, shedding light on neuron-specific pathophysiological mechanisms of BoDV-1 persistence and deciphering the signaling pathways linking DSB and neuronal activity are key to better understand the unique interaction of this RNA virus with its major target cell, the neuron.

Limitations of the study

Owing to low viral titers that are obtained with BoDV-1, experiments cannot be performed by infecting 100% of cells at once. Therefore, each neuron has likely been infected at a different stage during viral spread, which may explain in part the low DSB levels observed in this study, even when the culture is 100% infected.

STAR★METHODS

Detailed methods are provided in the online version of this paper and include the following:

- KEY RESOURCES TABLE
- RESOURCE AVAILABILITY
  - Lead contact
  - Material availability
  - Data and code availability
- EXPERIMENTAL MODEL AND SUBJECT DETAILS
  - Ethics statement
  - Virus stocks production
  - Primary cultures of neurons, virus infection and transduction by lentiviral vectors
  - Production and purification of lentiviral vectors
- METHOD DETAILS
  - Supernatants swapping
  - Single cell gel electrophoresis (Comet assay)
  - Western blot analysis
  - Indirect immunofluorescence analyses
  - Super-resolution analysis
  - Neuronal treatments
  - RT and qPCR for measurement of viral RNA
  - NMDAR immunostaining and quantification
  - Spontaneous electric activity recordings using nanoelectrode arrays, recording setup and activity analysis
  - SEM imaging
  - Blind-coding
- QUANTIFICATION AND STATISTICAL ANALYSIS

SUPPLEMENTAL INFORMATION

Supplemental information can be found online at https://doi.org/10.1016/j.isci.2021.103621.

REFERENCES

Akbarian, S., Beeri, M.S., and Haroutunian, V. (2013). Epigenetic determinants of healthy and diseased brain aging and cognition. JAMA Neurol. 70, 711–718.

Alt, F.W., Zhang, Y., Meng, F.L., Guo, C., and Schwer, B. (2013). Mechanisms of programmed DNA lesions and genomic instability in the immune system. Cell 152, 417–429.

Anderson, L., Henderson, C., and Adachi, Y. (2001). Phosphorylation and rapid relocalization of 53BP1 to nuclear foci upon DNA damage. Mol. Cell. Biol. 21, 1719–1729.

Baldock, R.A., Day, M., Wilkinson, O.J., Cloney, R., Jeggo, P.A., Oliver, A.W., Watts, F.Z., and Pearl, L.H. (2015). ATM localization and heterochromatin repair depend on direct interaction of the 53BP1-BRCT2 domain with gammaH2AX. Cell Rep. 13, 2081–2089.

Baudat, F., Imai, Y., and de Massy, B. (2013). Meiotic recombination in mammals: localization and regulation. Nat. Rev. Genet. 14, 794–806.

Bednarski, J.J., and Sleckman, B.P. (2019). At the intersection of DNA damage and immune responses. Nat. Rev. Immunol. 19, 231–242.

Betourne, A., Szelechowski, M., Thouard, A., Abrial, E., Jean, A., Zaidi, F., Foret, C., Bonnaud, E.M., Charlier, C.M., Suberbielle, E., et al. (2018). Hippocampal expression of a virus-derived protein impairs memory in mice. Proc. Natl. Acad. Sci. U S A. 115, 1611–1616.

Bonnaud, E.M., Suberbielle, E., and Malnou, C.E. (2016). Histone acetylation in neuronal (dys) function. Biomol. Concepts. 7, 103–116.

Bonnaud, E.M., Szelechowski, M., Betourne, A., Foret, C., Thouard, A., Gonzalez-Dunia, D., and Malnou, C.E. (2015). Borna disease virus phosphoprotein modulates epigenetic signaling in neurons to control viral replication. J. Virol. 89, 5996–6008.

Buxbaum, A.R., Wu, B., and Singer, R.H. (2014). Single beta-actin mRNA detection in neurons reveals a mechanism for regulating its translatability. Science 343, 419–422.

Casanova, A., Bettamin, L., Blatche, M.C., Mathieu, F., Martin, H., Gonzalez-Dunia, D., Nicu, L., and Larrieu, G. (2018). Nanowire based bioprobes for electrical monitoring of electrogenic cells. J. Phys. Condens. Matter 30, 464001.

Chen, T.I., Hsu, Y.K., Chou, C.Y., Chen, Y.H., Hsu, S.T., Liou, Y.S., Dai, Y.C., Chang, M.F., and Chang, S.C. (2019). Hepatitis C virus NS3 protein plays a dual role in WRN-mediated repair of nonhomologous end joining. J. Virol. 93, e01273-19.

Chevalier, G., Suberbielle, E., Monnet, C., Duplan, V., Martin-Blondel, G., Farrugia, F., Le Masson, G., Liblau, R., and Gonzalez-Dunia, D. (2011). Neurons are MHC class I-dependent targets for CD8 T cells upon neurotropic viral infection. PLoS Pathog. 7, e1002393.

Crowe, S.L., Movsesyan, V.A., Jorgensen, T.J., and Kondratyev, A. (2006). Rapid phosphorylation of histone H2A.X following ionotropic glutamate receptor activation. Eur. J. Neurosci. 23, 2351–2361.

Cubitt, B., and de la Torre, J.C. (1994). Borna disease virus (BDV), a nonsegmented RNA virus, replicates in the nuclei of infected cells where infectious BDV ribonucleoproteins are present. J. Virol. 68, 1371–1381.

Day, J.J., and Sweatt, J.D. (2011). Epigenetic mechanisms in cognition. Neuron 70, 813–829.

Enokido, Y., Yoshitake, A., Ito, H., and Okazawa, H. (2008). Age-dependent change of HMGB1 and DNA double-strand break accumulation in mouse brain. Biochem. Biophys. Res. Commun. 376, 128–133.

Ferre, C.A., Davezac, N., Thouard, A., Peyrin, J.M., Belenguer, P., Miquel, M.C., Gonzalez-Dunia, D., and Szelechowski, M. (2016). Manipulation of the N-terminal sequence of the Borna disease virus X protein improves its

mitochondrial targeting and neuroprotective potential. FASEB J. 30, 1523–1533.

Finck, T., Liesche-Starnecker, F., Probst, M., Bette, S., Ruf, V., Wendl, C., Dorn, F., Angstwurm, K., Schlegel, J., Zimmer, C., et al. (2020). Bornavirus encephalitis shows a characteristic magnetic resonance phenotype in humans. Ann. Neurol. 88, 723–735.

Galvan, S.C., Garcia Carranca, A., Song, J., and Recillas-Targa, F. (2015). Epigenetics and animal virus infections. Front. Genet. 6, 48.

Gonzalez-Dunia, D., Eddleston, M., Mackman, N., Carbone, K., and de la Torre, J.C. (1996). Expression of tissue factor is increased in astrocytes within the central nervous system during persistent infection with borna disease virus. J. Virol. 70, 5812–5820.

Hammack, C., Ogden, S.C., Madden, J.C., Jr., Medina, A., Xu, C., Phillips, E., Son, Y., Cone, A., Giovinazzi, S., Didier, R.A., et al. (2019). Zika virus infection induces DNA damage response in human neural progenitors that enhances viral replication. J. Virol. 93, e00638-19.

Hans, A., Bajramovic, J.J., Syan, S., Perret, E., Dunia, I., Brahic, M., and Gonzalez-Dunia, D. (2004). Persistent, noncytolytic infection of neurons by Borna disease virus interferes with ERK 1/2 signaling and abrogates BDNF-induced synaptogenesis. FASEB J. 18, 863–865.

Hirai, Y., Hirano, Y., Matsuda, A., Hiraoka, Y., Honda, T., and Tomonaga, K. (2016). Borna disease virus assembles porous cage-like viral factories in the nucleus. J. Biol. Chem. 291, 25789–25798.

Hristova, D.B., Lauer, K.B., and Ferguson, B.J. (2020). Viral interactions with non-homologous end-joining: a game of hide-and-seek. J. Gen. Virol. 101, 1133–1144.

Hu, H.L., Shiflett, L.A., Kobayashi, M., Chao, M.V., Wilson, A.C., Mohr, I., and Huang, T.T. (2019). TOP2beta-Dependent nuclear DNA damage shapes extracellular growth factor responses via

dynamic AKT phosphorylation to control virus latency. Mol. Cell 74, 466–480 e4.

Jie, J., Xu, X., Xia, J., Tu, Z., Guo, Y., Li, C., Zhang, X., Wang, H., Song, W., and Xie, P. (2018). Memory impairment induced by borna disease virus 1 infection is associated with reduced H3K9 acetylation. Cell Physiol. Biochem. 49, 381–394.

Khanna, M., Ray, A., Rawall, S., Chandna, S., Kumar, B., and Vijayan, V.K. (2010). Detection of influenza virus induced ultrastructural changes and DNA damage. Indian J. Virol. 21, 50–55.

Korn, K., Coras, R., Bobinger, T., Herzog, S.M., Lucking, H., Stohr, R., Huttner, H.B., Hartmann, A., and Ensser, A. (2018). Fatal encephalitis associated with borna disease virus 1. N. Engl. J. Med. 379, 1375–1377.

Koyama, T., Sun, B., Tokunaga, K., Tatsumi, M., and Ishizaka, Y. (2013). DNA damage enhances integration of HIV-1 into macrophages by overcoming integrase inhibition. Retrovirology 10, 21.

Lange, U.C., Verdikt, R., Ait-Ammar, A., and Van Lint, C. (2020). Epigenetic crosstalk in chronic infection with HIV-1. Semin. Immunopathol. 42, 187–200.

Lathe, R., and St Clair, D. (2020). From conifers to cognition: microbes, brain and behavior. Genes Brain Behav. 19, e12680.

Lau, C.G., Takayasu, Y., Rodenas-Ruano, A., Paternain, A.V., Lerma, J., Bennett, M.V., and Zukin, R.S. (2010). SNAP-25 is a target of protein kinase C phosphorylation critical to NMDA receptor trafficking. J. Neurosci. 30, 242–254.

Ledur, P.F., Karmirian, K., Pedrosa, C., Souza, L.R.Q., Assis-de-Lemos, G., Martins, T.M., Ferreira, J., de Azevedo Reis, G.F., Silva, E.S., Silva, D., et al. (2020). Zika virus infection leads to mitochondrial failure, oxidative stress and DNA damage in human iPSC-derived astrocytes. Sci. Rep. 10, 1218.

Li, N., Parrish, M., Chan, T.K., Yin, L., Rai, P., Yoshiyuki, Y., Abolhassani, N., Tan, K.B., Kiraly, O., Chow, V.T., et al. (2015). Influenza infection induces host DNA damage and dynamic DNA damage responses during tissue regeneration. Cell Mol. Life Sci. 72, 2973–2988.

Luftig, M.A. (2014). Viruses and the DNA damage response: activation and antagonism. Annu. Rev. Virol. 1, 605–625.

Madabhushi, R., Gao, F., Pfenning, A.R., Pan, L., Yamakawa, S., Seo, J., Rueda, R., Phan, T.X., Yamakawa, H., Pao, P.C., et al. (2015). Activity-induced DNA breaks govern the expression of

neuronal early-response genes. Cell 161, 1592–1605.

Mandke, P., and Vasquez, K.M. (2019). Interactions of high mobility group box protein 1 (HMGB1) with nucleic acids: implications in DNA repair and immune responses. DNA Repair (Amst). 83, 102701.

Mansuy, J.M., Suberbielle, E., Chapuy-Regaud, S., Mengelle, C., Bujan, L., Marchou, B., Delobel, P., Gonzalez-Dunia, D., Malnou, C.E., Izopet, J., et al. (2016). Zika virus in semen and spermatozoa. Lancet Infect. Dis. 16, 1106–1107.

Mao, K., and Zhang, G. (2021). The role of PARP1 in neurodegenerative diseases and aging. FEBS J. https://doi.org/10.1111/febs.15716.

Matsumoto, Y., Hayashi, Y., Omori, H., Honda, T., Daito, T., Horie, M., Ikuta, K., Fujino, K., Nakamura, S., Schneider, U., et al. (2012). Bornavirus closely associates and segregates with host chromosomes to ensure persistent intranuclear infection. Cell Host Microbe. 11, 492–503.

Niller, H.H., Angstwurm, K., Rubbenstroth, D., Schlottau, K., Ebinger, A., Giese, S., Wunderlich, S., Banas, B., Forth, L.F., Hoffmann, D., et al. (2020). Zoonotic spillover infections with Borna disease virus 1 leading to fatal human encephalitis, 1999-2019: an epidemiological investigation. Lancet Infect. Dis. 20, 467–477.

Olive, P.L., and Banath, J.P. (2006). The comet assay: a method to measure DNA damage in individual cells. Nat. Protoc. 1, 23–29.

Patra, T., Meyer, K., Ray, R.B., and Ray, R. (2020). Hepatitis C virus mediated inhibition of miR-181c activates ATM signaling and promotes hepatocyte growth. Hepatology 71, 780–793.

Piekna-Przybylska, D., Sharma, G., Maggirwar, S.B., and Bambara, R.A. (2017). Deficiency in DNA damage response, a new characteristic of cells infected with latent HIV-1. Cell Cycle 16, 968–978.

Ryan, E.L., Hollingworth, R., and Grand, R.J. (2016). Activation of the DNA damage response by RNA viruses. Biomolecules 6, 2.

Schlottau, K., Forth, L., Angstwurm, K., Hoper, D., Zecher, D., Liesche, F., Hoffmann, B., Kegel, V., Seehofer, D., Platen, S., et al. (2018). Fatal encephalitic borna disease virus 1 in solid-organ transplant recipients. N. Engl. J. Med. 379, 1377–1379.

Schmid, S., Metz, P., Prat, C.M., Gonzalez-Dunia, D., and Schwemmle, M. (2010). Protein kinase C-dependent phosphorylation of Borna disease virus P protein is required for efficient viral spread. Arch. Virol. 155, 789–793.

Skalka, A.M., and Katz, R.A. (2005). Retroviral DNA integration and the DNA damage response. Cell Death Differ. 12, 971–978.

Suberbielle, E., Djukic, B., Evans, M., Kim, D.H., Taneja, P., Wang, X., Finucane, M., Knox, J., Ho, K., Devidze, N., et al. (2015). DNA repair factor BRCA1 depletion occurs in Alzheimer brains and impairs cognitive function in mice. Nat. Commun. 6, 8897.

Suberbielle, E., Sanchez, P.E., Kravitz, A.V., Wang, X., Ho, K., Eilertson, K., Devidze, N., Kreitzer, A.C., and Mucke, L. (2013). Physiologic brain activity causes DNA double-strand breaks in neurons, with exacerbation by amyloid-beta. Nat. Neurosci. 16, 613–621.

Suberbielle, E., Stella, A., Pont, F., Monnet, C., Mouton, E., Lamouroux, L., Monsarrat, B., and Gonzalez-Dunia, D. (2008). Proteomic analysis reveals selective impediment of neuronal remodeling upon Borna disease virus infection. J. Virol. 82, 12265–12279.

Tarakhovsky, A., and Prinjha, R.K. (2018). Drawing on disorder: How viruses use histone mimicry to their advantage. J. Exp. Med. 215, 1777–1787. https://doi.org/10.1084/jem.20180099.

Torres, G., Leheste, J.R., and Ramos, R.L. (2015). Immunocytochemical localization of DNA double-strand breaks in human and rat brains. Neuroscience 290, 196–203.

Tsai, K., and Cullen, B.R. (2020). Epigenetic and epitranscriptomic regulation of viral replication. Nat. Rev. Microbiol. 18, 559–570.

van den Berg, J., Manjón, A.G., Kielbassa, K., Feringa, F.M., Freire, R., and Medema, R.H. (2018). A limited number of double-strand DNA breaks is sufficient to delay cell cycle progression. Nucleic Acids Res. 46, 10132–10144.

Vieira, M., Yong, X.L.H., Roche, K.W., and Anggono, V. (2020). Regulation of NMDA glutamate receptor functions by the GluN2 subunits. J. Neurochem. 154, 121–143.

Volmer, R., Monnet, C., and Gonzalez-Dunia, D. (2006). Borna disease virus blocks potentiation of presynaptic activity through inhibition of protein kinase C signaling. PLoS Pathog. 2, e19.

Weitzman, M.D., and Fradet-Turcotte, A. (2018). Virus DNA replication and the host DNA damage response. Annu. Rev. Virol. 5, 141–164.

Wyllie, D.J., Livesey, M.R., and Hardingham, G.E. (2013). Influence of GluN2 subunit identity on NMDA receptor function. Neuropharmacology 74, 4–17.

STAR★METHODS

KEY RESOURCES TABLE

REAGENT or RESOURCE	SOURCE	IDENTIFIER
Antibodies		
Mouse monoclonal anti-γH2A.X	ThermoFisher	Cat#MA1-2022; RRID: AB_559491
Mouse monoclonal anti-γH2A.X, clone JBW301	Sigma	Cat#05-636; RRID: AB_309864
Mouse monoclonal anti-β-Actin	Sigma	Cat#A5441; RRID: AB_476744
Mouse monoclonal anti-α-Tubulin	Sigma	Cat#T6199; RRID: AB_477583
Mouse monoclonal anti-GFP	Millipore	Cat#MAB3580; RRID: AB_94936
Mouse polyclonal anti-Nucleoprotein	Homemade	N/A
Mouse monoclonal anti-Nucleoprotein (Bo18)	Gift from Christiane Herden	N/A
Rabbit polyclonal anti-Nucleoprotein	Homemade	N/A
Mouse polyclonal anti-Phosphoprotein	Homemade	N/A
Rabbit polyclonal anti-Phosphoprotein	Homemade	N/A
Rabbit polyclonal anti-X	Homemade	N/A
Rabbit polyclonal anti-53BP1	Novus	Cat#NB100-304; RRID: AB_10003037
Mouse monoclonal anti-MAP2	Sigma	Cat#M1406; RRID: AB_477171
Chicken polyclonal anti-MAP2	Abcam	Cat#ab5392; RRID: AB_2138153
Rabbit polyclonal anti-GluN2A	Invitrogen	Cat#480031; RRID: AB_2532251
Alexa Fluor 488 Goat anti-Mouse	Thermo	Cat#A11029; RRID: AB_138404
Alexa Fluor 488 Goat anti-Rabbit	Thermo	Cat#A11034; RRID: AB_2576217
Alexa Fluor 555 Goat anti-Rabbit	Thermo	Cat#A27039; RRID: AB_2536100
Alexa Fluor 594 Goat anti-Mouse	Thermo	Cat#A11032; RRID: AB_2534091
Alexa Fluor 594 Goat anti-Rabbit	Thermo	Cat#A11037; RRID: AB_2534095
Alexa Fluor 633 Goat anti-Chicken	Thermo	Cat#A21103; RRID: AB_1500591
Abberior® STAR RED Goat anti-Rabbit	Abberior	Cat#41699; RRID:AB_2833015
Abberior® STAR RED Goat anti-Mouse	Abberior	Cat# STRED-1001; RRID:AB_2810982
CF®770 Goat anti-Mouse	Biotium	Cat#20077; RRID: AB_10852670
CF®680 Goat anti-Rabbit	Biotium	Cat#20067; RRID: AB_10871686
Bacterial and virus strains		
BoDV-1 He/80 strain	Cubitt and de la Torre (1994)	GenBank: L27077
Biological samples		N/A
Chemicals, peptides, and recombinant proteins		
Papaïn	Worthington	Cat#LK003178
Bovine Serum Albumin (BSA)	Euromedex	Cat#04-100-811-0
Trypsin inhibitor from chicken egg white	Sigma	Cat#T2011; CAS: 9035-81-8
DNAse I recombinant grade I	Roche	Cat#04536282001
Neurobasal Medium	Gibco	Cat#12348-017
B-27 supplement 50X	Thermo	Cat#17504-44
Penicillin-Streptomycin	Thermo	Cat#151140-122
GlutaMAX	Gibco	Cat#13462629
Poly-DL-ornithine hydrobromide	Sigma	Cat#P8638; CAS: 82682-33-5
Natural Mouse Laminin	Thermo	Cat#23017-015

(Continued on next page)

Continued

REAGENT or RESOURCE	SOURCE	IDENTIFIER
OptiMEM	Gibco	Cat#11058
GeneJuice® Transfection Reagent	Merck	Cat#70967-4; CAS: 64-17-5
Hank's Balanced Salt Solution (HBSS)	Gibco	Cat#14175-053
DMEM+glutaMAX	Gibco	Cat#31966-021
Dimethyl Sulfoxide Salt Solution (DMSO)	Sigma	Cat#D8418; CAS: 67-68-5
Etoposide (ETP)	Sigma	Cat# E1383; CAS: 33419-42-0
N-Methyl-D-aspartic acid (NMDA)	Sigma	Cat#M3262; CAS: 6384-92-5
2,3-dioxo-6-nitro-7-sulfamoyl-benzo[f] quinoxaline (NBQX)	Tocris	Cat#1044; CAS: 479347-86-9
Phosphatase inhibitor cocktail 2	Sigma	Cat#P5726
Phosphatase inhibitor cocktail 3	Sigma	Cat#P0044; EC: 200-664-3
Complete, Mini, EDTA-free, protease inhibitor	Roche	Cat#1183617001
Intercept Odyssey (TBS) Blocking Buffer	LI-COR	Cat#927-60003
Paraformaldéhyde 32%	Euromedex	Cat#15714
Normal Goat Serum	Thermo	Cat#31873
DAPI	Sigma	Cat#D9542; CAS: 28718-90-3
ProLong Gold antifade reagent	Thermo	Cat#P36934
Critical Commercial Assays		
Monarch® Total RNA Miniprep Kit	New England BioLabs	Cat#T2010S
LunaScript™ RT SuperMix Kit	New England BioLabs	Cat#E3010G
Light-Cycler 480 DNA SYBR green I Master reaction mix	Roche	Cat#4887352001
Click-iT Plus TUNEL Assay for In Situ Apoptosis Detection, Alexa Fluor 594 dye	Thermo	Cat#C10618
CometAssay® Kit (25 x 2 Well CometSlides)	Trevigen	Cat#4250-050-K
Experimental models: Cell lines		
Vero Cells	ATCC	Cat#CCL-81
HEK293T Cells	ATCC	Cat#CRL-3216
Experimental models: Organisms/strains		
E16 to E18 Embryos brain from pregnant SPRAGUE-DAWLEY rats	Janvier LABS	Cat#RN-SD-F
Oligonucleotides		
Primer: GAPDH (Forward) TGCTGGTGCTGAGTATGTCG	This paper	N/A
Primer: GAPDH (Reverse) GGCGGAGATGATGACCCTTT	This paper	N/A
Primer: BoDV-1 cDNA (Forward) CCTTCTAACAAAATGAATACACGC	This paper	N/A
Primer : BoDV-1 cDNA (Reverse) CTGATATCCTTCTCATGCCC	This paper	N/A
Recombinant DNA		
Plasmid psPAX2	Gift from Didier Trono	Addgene plasmid #12260
		RRID:Addgene_12260
Plasmid pMD2.G	Gift from Didier Trono	Addgene plasmid #12260
		RRID:Addgene_12259

Continued

REAGENT or RESOURCE	SOURCE	IDENTIFIER
Plasmid pTRIP-N	Gift from Pierre Charneau	N/A
Plasmid pTRIP-P	Gift from Pierre Charneau	N/A
Plasmid pTRIP-X	Gift from Pierre Charneau	N/A
Plasmid pTRIP-GFP	Gift from Pierre Charneau	N/A
Software and algorithms		
CometScore	RexHoover/Tritek	http://rexhoover.com/index.php?id=cometscore
FIJI	ImageJ	https://imagej.net/Fiji; RRID: SCR_002285
GraphPad Prism 8	GraphPad	https://www.graphpad.com/scientific-software/prism/; RRID:SCR_002798
MATLAB	MathWorks	https://fr.mathworks.com/products/matlab.html; RRID: SCR_001622
LabViEW	Homemade	N/A
Huygens Professional	SVI	https://svi.nl/HuygensSoftware; RRID: SCR_014237
Imaris	Bitplane AG	https://imaris.oxinst.com/packages; RRID: SCR_007370
ImageStudio	LI-COR	https://www.licor.com/bio/image-studio/; RRID: SCR_015795

RESOURCE AVAILABILITY

Lead contact

Further information and requests for resources and reagents should be directed to and will be fulfilled by the lead contact, Elsa Suberbielle (elsa.suberbielle@inserm.fr)

Material availability

This study did not generate new unique reagents.

Data and code availability

All data reported in this paper will be shared by the lead contact upon request.

This paper does not report original code.

Any additional information required to reanalyze the data reported in this paper is available from the lead contact upon request.

EXPERIMENTAL MODEL AND SUBJECT DETAILS

Ethics statement

Animal handling and care for the preparation of primary neuronal cultures from rat embryos were performed in accordance with European Union Council Directive 86/609/EEC, and experiments were performed following the French national chart for ethics of animal experiments (articles R 214-87 to -90 of the "Code rural"). Our protocol received approval from the local committee on the ethics of animal experiments (permit number PI-U1043-DD-10). Pregnant rats were deeply anesthetized with CO_2 before euthanasia to minimize suffering.

Virus stocks production

Cell-released virus stocks were prepared using Vero cells persistently infected by wild-type BoDV-1 (Giessen strain He/80) and as previously described (Schmid et al., 2010). Confluent flasks of cells were

shocked by a hypertonic solution containing 20 mM Hepes buffer, 250 mM MgCl$_2$ and 1% fetal bovine serum (FBS, Sigma). Culture supernatants were then clarified with two centrifugations at 2000 g and finally filtered at 0.45 μm. Supernatants were ultracentrifuged on a 20% sucrose gradient in PBS at 100,000 g at 4°C. Virus-containing pellets were resuspended in Neurobasal medium and, after brief sonication to facilitate particles solubilization, aliquoted and stored at −80°C.

Primary cultures of neurons, virus infection and transduction by lentiviral vectors

Primary hippocampal neurons were prepared from Sprague-Dawley rat embryos at gestational day E16 to E18 by a papain dissociation method as described previously (Chevalier et al., 2011). Cells from male and female embryos were mixed cultures in absence of sex determination before birth. Briefly, hippocampi from the embryo's brain were dissected out and dissociated by papain (Worthington) digestion and mechanic homogenization. Papain digestion was stopped with a solution containing bovine serum albumin (BSA, Euromedex), a protease inhibitor (Trypsin inhibitor from chicken egg, Merck) and DNAse (Roche). Cell homogenates were resuspended in neuronal medium and purified by centrifugation on 4% BSA in neuronal medium to eliminate glial cells. Neurons were plated on poly-ornithine- (Sigma) and laminin- (Thermoscientific) coated dishes. They were cultivated at a density of 0.5x10^6 neurons per well in 12-well plates to prepare protein/RNA extracts, or at a density of 1.3x10^5 neurons per well in 24-well plates containing coverslips for immunofluorescence staining. Neurons were maintained in Neurobasal medium supplemented with 2% B-27 supplement, 1.2% GlutaMAX and 120 U: 120 μg/mL of Penicillin: Streptomycin (Life Technologies). Neurons were infected with BoDV-1 (He/80 Giessen strain) at DIV1, DIV7 or DIV9 (according to the experiments) using a Multiplicity Of Infection (MOI) of 0.03. Neurons were transduced by lentiviral vectors at DIV7 at a MOI of 3 for high-density cultures or 0.5 for low-density cultures. Neurons were maintained in culture 2 weeks before analyses, or as specified in each experiment.

Production and purification of lentiviral vectors

HEK293T cells (ATCC CRL-3216) were co-transfected with three plasmids: pMD2.G plasmid encoding the vesicular stomatitis virus envelope glycoprotein (VSV-G, Addgene plasmid 12259, donated by D. Trono), psPAX2 packaging plasmid (Addgene plasmid 12260, donated by D. Trono) and one of the following plasmids coding a BoDV-1 protein or GFP: pTRIP-N, p-TRIP-P, pTRIP-X or pTRIP-GFP (Bonnaud et al., 2015; Ferre et al., 2016) ; using transfection reagent (Genejuice, Millipore). 24 h later, medium was replaced by OptiMEM (Life technologies) medium containing 100 U: 100 μg/mL of Penicillin: Streptomycin. After 24 h and 48 h, supernatants containing lentiviral vectors were harvested, clarified by centrifugation at 2,000 g and then filtered at 0.45 μm. Supernatants were ultracentrifuged on a 20% sucrose cushion in PBS at 100,000 g at 4°C. Lentiviral vectors pellets were resuspended in HBSS buffer, aliquoted and stored at −80°C.

METHOD DETAILS

Supernatants swapping

Two weeks post-infection, supernatants were collected from each well for a given condition, pooled, filtered on a 0.22 μm filter (ClearLine). 1 mL of the filtered supernatant from mock-infected cultures was added onto non-infected cultures, and 1mL of filtered supernatant from infected cultures was added onto non-infected and infected cultures. After 5 hours of incubation, proteins were extracted for Western blot analysis.

Single cell gel electrophoresis (Comet assay)

Comet assay was carried out at neutral pH to analyze DSB using the CometAssay kit (Trevigen), according to the manufacturer's instructions and as described in Suberbielle et al. (2013). Briefly, nuclei were extracted from 14 DIV neuronal cultures in 12-well dishes, using ice-cold PBS 1X. 10^5 nuclei/ml were combined with low melting point agarose at a 1:10 ratio. Comet assays were performed at neutral pH (pH 8.3), because this condition makes the assay more specific for the detection of DSB (Olive and Banath, 2006). Single-cell gel electrophoresis was performed in TAE buffer at 1 V/cm for 40 min. SYBR-green was used to stain the comet-like smears of DNA fragments that emerged from cells containing DSB. Digitized images were obtained with a Zeiss Wide field Apotome 2 microscope using the tile tool of the Zen blue software at the 5x Objective. Tiles were stitched with the software and resulting bitmap-formatted images of the entire Cometslide™ well were analyzed with the free CometScore software (Tritek). For each sample, the number of cells with comets was counted automatically by the software and normalized to the total

number of cells. The total number of cells was manually counted using the cell counter plugins from FIJI. For each well, at least 250 cells were inspected. For each comet shape detected, the comet was automatically framed and a cursor adjusted on the head of the comet. All comet event were double-checked manually. The software automatically determined the tail length and Tail moment using a built-in algorithm for comet scoring. For each well, the experimenter calculated the average values of the tail length and the tail moment.

Western blot analysis

After rinsing cells with 1X phosphate buffer saline (PBS) at room temperature, neurons were lysed on ice using ice-cold RIPA buffer containing Tris-HCl pH 7.5 (50 mM), NaCl (150 mM), NP40 (1%), Sodium deoxycholate (12 mM) and SDS (0.1%); completed by Complete mini protease inhibitor (Roche) and cocktails 2 and 3 of phosphatase inhibitors (Sigma) and then sonicated. The lysates were centrifugated at 4°C to eliminate debris and the supernatants were stored at −20°C. Proteins extracts were loaded on 4-15% Bis-Tris gels (BioRad), separated by SDS-PAGE and then transferred onto 0.22 μm nitrocellulose membranes. Membranes were blocked with Odyssey blocking buffer (Li-COR) or 5% (wt/vol) non-fat dry milk in TBS and incubated with primary antibodies for 3 h at room temperature, or overnight at 4°C, using the following antibodies: mouse anti-γH2A.X monoclonal, dilution 1/1,000 (ThermoFisher, MA1-2022), mouse anti-β-Actin monoclonal, dilution 1/50,000 (Sigma, A5441), mouse anti-α-Tubulin monoclonal, dilution 1/10,000 (Sigma, T6199), rabbit anti-GFP polyclonal, dilution 1/2,000 (ThermoFisher, A-11122), rabbit anti-N polyclonal antibody, dilution 1/50,000 (homemade), rabbit anti-P polyclonal antibody, dilution 1/50,000 (homemade), rabbit anti-X polyclonal antibody, dilution 1/10,000 (gift by K. Tomonaga and M. Schwemmle) in Odyssey blocking buffer or TBS containing 0.1% (vol/vol) Tween-20 (TBS-T) and 5% non-fat milk. Membranes were incubated with corresponding secondary antibodies coupled with infrared fluorescent dye (CF680 and CF770, Biotium) 1/10,000 diluted in Odyssey blocking buffer or in TBS-T with 5% non-fat milk TBS. Western blot signals were analyzed using an Odyssey Li-COR infrared imaging system coupled with Image studio software (Li-COR). All protein signals were normalized on the β-Actin signal except for the experiments depicted in Figure 5. In these experiments, protein signals were normalized on α-Tubulin signals, since stimulation of neuronal activity may impact on β-Actin protein expression (Buxbaum et al., 2014).

Indirect immunofluorescence analyses

Neurons on coverslips were fixed with 4% paraformaldehyde (PFA) solution in PBS during 15 min at room temperature, rinsed twice with Tris-Buffered Saline (TBS) and permeabilized with TBS-0.05% Triton X100 during 5 min. After washings with TBS, coverslips were incubated in blocking solution (5% Normal Goat Serum (NGS) in 0.05% TBS-Tween20) 1 h at room temperature or overnight at 4°C and then incubated with primary antibodies 3 h at room temperature or overnight at 4°C. Antibodies used were as follows: mouse anti-GFP monoclonal, dilution 1/500 (Millipore, MAB3580), mouse anti-γH2A.X monoclonal clone JBW301, dilution 1/300 for STED analyses (Sigma-Aldrich, 05-636), mouse anti-N polyclonal antibody, dilution 1/2,000 (gift from C. Herden), mouse anti-N monoclonal antibody (Bo18), dilution 1/100 (generously provided by Christiane Herden), mouse anti-P polyclonal antibody, dilution 1/500 (homemade), mouse anti-X polyclonal antibody, dilution 1/500 (gift by K. Tomonaga and M. Schwemmle), rabbit anti-N polyclonal antibody, dilution 1/1,5000 (homemade), rabbit anti-53BP1 polyclonal, dilution 1/1,000 (Novus, NB100-304), chicken anti-MAP2 polyclonal, dilution 1/2,000 (Abcam, ab5392), in 0.05% TBS-Tween20 containing 3% NGS. Cells were washed 3 times with 0.05% TBS–Tween20 and incubated with corresponding dye-conjugated secondary antibodies diluted in 0.05% TBS-Tween20 containing 3% NGS for 1 h at room temperature or overnight at 4°C. Secondary antibodies were conjugated to Alexa- (Alexa Fluor 488, 555, 594, 633, Life technologies) or dye StarRed- (750, Abberior) dyes. Finally, nuclei were stained using DAPI during 10 min at room temperature and coverslips were mounted on a slide with ProLong Gold Antifade mounting medium (Life Technologies) or homemade MOWIOL for STED analysis.

Neurons with 53BP1-positive foci were counted using the 40X objective of an Olympus BX41 fluorescence microscope equipped with an X-Cite UV light source, as follows: 2 to 4 fields were counted per coverslip ; 2 to 3 coverslips were considered per condition and per experiment. Between 500 to 1,000 neurons were analyzed per condition and per experiment. For each field, the total number of neurons and the number of neurons presenting at least one focus were counted. For the experiments after Etoposide treatment, neurons presenting at least one focus of 53BP1 and at least one vSPOT were randomly counted, analyzing z-stacks acquisitions taken by confocal microscopy on Leica SP8 confocal microscope (Leica Microsystems, Germany) processed on FIJI software. In total, around 200 neurons were counted per condition. The illustrations of immunofluorescence figures (excepting

STED experiment) are issued from z acquisitions performed on Leica SP8 confocal microscope followed by standard deviation projection using FIJI software.

Super-resolution analysis

Super-resolution stimulated emission depletion (SR-STED) microscopy images were acquired using a Leica SP8 STED 3× microscope (Leica Microsystems, Germany) and a 100× NA: 1.4 oil immersion objective, as previously used in (Mansuy et al., 2016). To optimize the resolution without bleaching in 3D, the 775 nm STED laser line was applied at the lowest power that could provide sufficient improvement in resolution compared with confocal. z-stack series were acquired sequentially with the pulsed 532 nm laser line and the pulsed 635 nm laser line. With such settings, lateral and axial resolutions of 130 nm could be reached for both acquisition channels. For image acquisition, we used the following parameters: 43 nm pixel size, two-time average par line, 400 Hz scan speed. The z-stacks of 25 neuronal nuclei presenting DSB were randomly acquired per experiment and 3 independent experiments were run (z-step: 40nm). The z-stacks were screened with the merged z-stack display on the Leica SP8 LSM software to count the number of DSB per nucleus, vSPOT per nucleus and the number of colocalization events. STED images were subsequently deconvolved with Huygens Professional (SVI, USA) using the CMLE algorithm, with a signal-to-noise ratio (SNR) of 7. Three-dimensional visualization and reconstruction using Imaris software (Bitplane AG, Switzerland) were used to measure the distance between 53BP1 positive foci of DSB and vSPOT in the nuclei of neurons. Imaris software was used to automatically identify vSPOT and 53BP1 foci and calculate the shorter distances between them, after thresholding and 3D reconstruction. Co-localization of vSPOT or 53BP1 foci with γH2A.X were also performed to identify DSB that are more recently formed (Baldock et al., 2015). After 3D-reconstructions, movies were also generated from an example of colocalization. Illustrations were obtained by maximal projection of 3D confocal STED z-stacks images after deconvolution.

Neuronal treatments

All stimulations were done at DIV14, after pre-treating neurons with 20 μM NBQX (Tocris) during 30 min, to inhibit non-NMDA-type glutamate receptors. To achieve global activation of N-methyl-D-aspartate receptors (NMDAR), after washing cells with 1X PBS at 37°C, neurons were stimulated with 15 μM NMDA (Sigma) in pre-warmed conditioned media during 30 min. To study the link between DSB and viral replication, infected neurons were treated with various concentration of Etoposide (ETP; Sigma) in DMSO, 2 days post-infection (dpi) during 5 days (vSPOT and DSB analysis), or treated 5 dpi during 24, 48, 72 hours (viral RNA (vRNA) analysis). The same final concentration of DMSO treatment was used as negative control. All drugs were applied directly to the medium, and the neurons were maintained at 37°C with 5% CO_2 during all treatments.

RT and qPCR for measurement of viral RNA

At DIV9, neurons were infected by BoDV-1 at MOI = 0.03. 5 days post-infection, neurons were treated with ETP at 0.5 μM or with DMSO alone. 24, 48 or 72 hours after treatment, total RNA was extracted. Total RNA was prepared from cells using a Monarch® Total RNA Miniprep Kit (New England BioLabs) according to the manufacturer's instructions. Total RNA was reverse transcribed using LunaScript™ RT SuperMix Kit (New England BioLabs). Quantitative PCR was performed on cDNAs using sets of primers specific for glyceraldehyde-3-phosphate dehydrogenase (GAPDH) for normalization (forward primer, 5' TGCTGGTGCTGA GTATGTCG 3'; reverse primer, 5' GGCGGAGATGATGACCCTTT 3') or with primers specific for viral cDNA (forward primer, 5' CCTTCTAACAAAATGAATACACGC 3'; reverse primer, 5' CTGATATCCTTCTCA TGCCC 3'). qPCRs mix were made using Light-Cycler 480 DNA SYBR green I Master reaction mix (Roche Diagnostics) and run in duplicates using a LightCycler 480 instrument (Roche Diagnostics). PCR cycles were as follows: after an initial incubation at 95°C for 5 min, 40 amplification cycles were run (at 95°C for 10 s, 60°C for 15 s, then 72°C for 15 s) followed by melting curve analysis. Viral genome quantification was expressed in arbitrary units according to the following threshold cycle (CT) formula: amount of viral RNA = $2^{-(Ct^{BoDV} - Ct^{GAPDH})}$.

NMDAR immunostaining and quantification

To stain for surface NMDAR only, neurons on coverslips were incubated with rabbit anti-GluN2A polyclonal antibody, at a dilution of 1/100 (Invitrogen, #480031) in cold Tyrode medium: NaCl (119 mM), KCl (5 mM), $CaCl_2$ (2 mM), $MgCl_2$ (2 mM), Hepes (25 mM), glucose (30 mM) on ice during 45 min. Then, the coverslips were washed three times in cold 1X PBS and incubated for 15 min on ice, in a solution of 4% PFA in PBS. Following a step of permeabilization and blocking, immunofluorescence stainings were performed as

previously described. Coverslips were stained with anti-MAP2 antibody and, to detect total GluN2A signals, part of them was stained with anti-GluN2A antibody, overnight at 4°C. High-resolution z-stacks of images were generously acquired by Zeiss France representative in airyscan mode using a Zeiss LSM 980 with Airyscan 2, using all identical parameters between samples. Images represents the maximal projection of 4 confocal planes (step: 0.169 μm). Quantification of GluN2A expression was performed from z-stacks acquisitions, at the 63× objective with a zoom factor of 3, taken by confocal microscopy on Leica SP8 confocal microscope. Identical settings for laser power, photomultiplier gain and offset were used for all experiments. Neurons were randomly selected, but those grouped in clusters and without detectable distinct neurites were excluded, to avoid bias in measurements of potential overlapping neurites. On the GluN2A channel, images were analyzed on FIJI software: after stack summation, the background was subtracted using the rolling ball and sliding paraboloid tools of the software. Regions Of Interest (ROI) were manually drawn on the projection of MAP2 staining to define neurites regions and measure their area. GluN2A projections were thresholded to include all the GluN2A signals grouped as clusters. Clusters were defined as groups of at least 3 pixels. Particles measuring less than 3 pixels were arbitrarily considered as not representative of a GluN2A cluster and were excluded from the measurements. The ROI were used to measure the thresholded GluN2A signal. The results were finally presented as intensity per $μm^2$ of neurites. 2 to 7 neurites were analyzed from 3 to 7 neurons over 2 coverslips per condition, in 3 independent experiments, for GluN2A surface and total quantifications. In average, were assessed 74 vs. 84 (NI vs. BoDV) dendrites for surface expression of GluN2A and 102 vs. 94 (NI vs. BoDV) dendrites for total expression of GluN2A.

Spontaneous electric activity recordings using nanoelectrode arrays, recording setup and activity analysis

The nanoelectrode array devices were fabricated in the LAAS-CNRS clean room, using a series of micro-technology processes compatible with a large-scale type of fabrication (Casanova et al., 2018). Briefly, the device is composed of a cultured chamber (well) containing 60 nano-electrodes composed by 3D nanowires coated with a platinum silicide (PtSi) biocompatible surface. Each electrode is electrically isolated thanks to an oxide layer. The recording setup was also mainly developed at the LAAS. It is composed of an MEA holder (MEA1060-Inv-BC from Multichannel System), a homemade electronic card where the integrated electronics allows to control the system and an acquisition card (USB 6353 from National Instruments). The recording setup is controlled by a homemade software developed on LabVIEW that allows live recordings on multiple channels, saving the data and performing online data treatment such as filtering and averaging. The cell recordings were performed with neurons maintained inside an incubator at 37°C with controlled humidity and 5% CO_2. Each electrode was recorded 5 to 6 times during 3 minutes in groups of 15 electrodes, one group after the other in 3 independent experiments (1 well of 60 electrodes per condition). Once the data were acquired, a MATLAB script was used for the offline treatment. A peak detection algorithm was used to evaluate the frequency of activation of each electrode. The threshold for the peak detection was calculated using the standard deviation of the background noise. Electrodes presenting aberrant recordings were excluded. Active electrodes were considered as electrodes where at least one peak was recorded.

SEM imaging

Cells were fixed with 5% glutaraldehyde in PBS overnight at 4°C, rinsed 3 times with PBS 1X and dehydrated by graded series of ethanol and dried at room temperature. Images of the cell cultures are done with a Scanning Electron Microscope (Helios 600i).

Blind-coding

Investigators who obtained data were blinded to infection and treatment of cell cultures.

QUANTIFICATION AND STATISTICAL ANALYSIS

Sample sizes were chosen on the basis of pilot experiments and our experience with similar experiments. Statistical analyses were performed with Prism 8 (GraphPad). Normal distribution of the data was verified with D'Agostino and Pearson's omnibus normality test and Bartlett-test was used to verify equality of variance. Welch's correction was applied when the variances were not equal. Each statistical test is specified in the legend of each figure. Null hypotheses were rejected at the 0.05 level.